SANDIA REPORT

SAND2022-13342
Printed September, 2022

Sandia National Laboratories

System Response Characterization for a d-t Neutron Radiography System

P. Marleau, K. Sjoberg, M. Sweany, and K. Weinfurther

Prepared by
Sandia National Laboratories
Albuquerque, New Mexico 87185
Livermore, California 94550

Issued by Sandia National Laboratories, operated for the United States Department of Energy by National Technology & Engineering Solutions of Sandia, LLC.

Available to DOE and DOE contractors from

U.S. Department of Energy
Office of Scientific and Technical Information
P.O. Box 62
Oak Ridge, TN 37831

Telephone: (865) 576-8401
Facsimile: (865) 576-5728
E-Mail: reports@osti.gov
Online ordering: http://www.osti.gov/scitech

Available to the public from

U.S. Department of Commerce
National Technical Information Service
5301 Shawnee Road
Alexandria, VA 22312

Telephone: (800) 553-6847
Facsimile: (703) 605-6900
E-Mail: orders@ntis.gov
Online order: https://classic.ntis.gov/help/order-methods

ABSTRACT

We report the system response of a pixelated associated particle imaging (API) neutron radiography system. The detector readout currently consists of a 2x2 array of organic glass scintillator detectors, each with an 8x8 array of optically isolated pixels that match the size and pitch of the ARRAYJ-60035-64P-PCB Silicon Photomultiplier (SiPM) array from SensL/onsemi with 6x6 mm^2 SiPMs. The alpha screen of the API deuterium-tritium neutron generator is read out with the S13361-3050AE-08 from Hamamatsu, which is an 8x8 array of 3x3 mm^2 SiPMs. Data from the 320 channel system is acquired with the TOFPET2-based readout system. We present the predicted imaging capability of an eventual 5x5 detector array, the waveform-based energy and pulse shape characterization of the individual detectors, and the timing and energy response from the TOFPET2 system.

ACKNOWLEDGMENT

The authors would like to thank Annabelle Benin, Patrick Feng, and Huu Tran of Sandia National Laboratories for construction of the OGS arrays. Scott Kiff provided an independent technical review of this work.

Sandia National Laboratories is a multimission laboratory managed and operated by National Technology and Engineering Solutions of Sandia, LLC, a wholly owned subsidiary of Honeywell International, Inc., for the U.S. Department of Energy's National Nuclear Security Administration under contract DE-NA0003525. This paper describes objective technical results and analysis. Any subjective views or opinions that might be expressed in the paper do not necessarily represent the views of the U.S. Department of Energy or the United States Government.

CONTENTS

LIST OF FIGURES

LIST OF TABLES

NOMENCLATURE

Table 0-1.

Abbreviation	Definition
API	Associated Particle Imaging
CT	Computed Tomography
d-t	deuterium-tritium
DOE	Department of Energy
ESR	Enhanced Specular Reflector
FoM	Figure of Merit
GUI	Graphical User Interface
OGS	Organic Glass Scintillator
PMT	photomultiplier tube
PSCD	Parabolical Surrogate Coordinate Descent
PSD	Pulse Shape Discrimination
SiPM	Silicon Photomultipler
SNL	Sandia National Laboratories

1. INTRODUCTION

Neutron imaging enables the geometrical characterization of fissioning nuclear material in the case of passive imaging, or the nuclear density and even elemental fractions of intervening material in the case of active imaging. Imaging systems often require a pixelated neutron detector plane. Positional information for the detection plane of the Neutron Coded Aperture system [1, 2, 3] and the Advanced Portable Neutron Imaging System [4] is obtained using Anger-logic readout [5]. Each position-sensitive detector consists of a 10x10 array of 1.08x1.08x5 cm^3 segments of pulse shape discrimination (PSD)-capable plastic scintillator from Eljen (EJ-299-34). The segments are individually wrapped with a layer of 3M's Enhanced Specular Reflector (ESR) material, which achieves nearly 98% specular reflectivity in the 380-800 ns wavelength range [6]. The scintillator block is read out by four 2" Hamamatsu R7724-100 super bialkali photomultiplier tubes. The detectors include a thermal neutron detection material ^{6}Li/ZnS:Ag. ZnS:Ag has a phosphorescence response to the particles (α, t) released by neutron capture on lithium-6. Because of its comparatively long decay time, phosphorescence is easily distinguished from both neutron and gamma induced scintillation in EJ-299-34 using pulse-shape discrimination techniques.

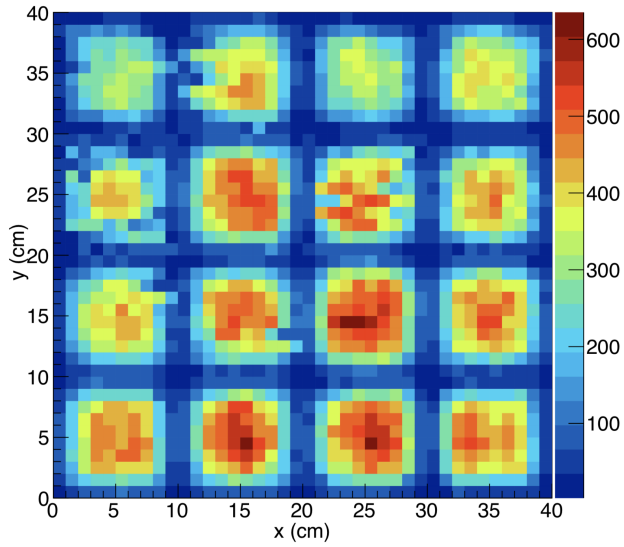

Figure 1-1. The neutron response to a uniform flood of particles for a 4x4 array of 10x10 cm^2 pixelated neutron detectors using Anger logic readout. The non-uniform response is in part due to the non-uniform light collection efficiency of each pixel, resulting in highly degraded PSD for pixels on the edge of each detector. This greatly reduces the neutron detection efficiency for pixels near the edge of each detector compared to pixels near the center.

While offering a cost-effective solution to reduce acquisition channels, this method prevents the ability to determine whether a neutron scattered multiple times within the detector: the

reconstructed interaction position will be a combination of all depositions within the acquisition time window, leading to artifacts in the reconstructed image. In addition, the current position-sensitive detector limits the detection efficiency for single neutron depositions. The greatest source of inefficiency in the current design is due to non-uniform light collection across the pixel plane. This is illustrated by Figure 1-1, in which the neutron response to a flood of particles is shown for a 4x4 array of detectors: the drop in detection efficiency for edge pixels is evident by the drop in detection rate compared to pixels near the center of each detector. Prior experimental-based estimates indicate that independent readout of each pixel could allow a detector one quarter of the size to retain up to 76% of the detection efficiency of the 10x10x5 cm^3 block detector and have 3x the number of single scatter-resolved events [7]: this estimate takes into account the fraction of fission-energy neutrons that have multiple scatters, as well as detection improvements due to improved light collection efficiency, however do not account for possible reductions in the fraction of multiple scatter events due to reduced volume.

Advances in Silicon Photomultiplier (SiPM) technology makes highly pixelated photo-detection with $O(100)$ ps timing feasible, allowing for cost effective independent pixel readout and the ability to resolve multiple scatters that occur within less than 1 ns. We recently reported on an evaluation of several different pixelated organic scintillator technologies designed to couple to SensL/onsemi's 8x8 array of 6x6 mm^2 J-series SiPMs (ARRAYJ-60035-64P-PCB) [8]. Light collection, energy resolution, and optical cross talk were evaluated to determine how much light is reaching the photodetector and remaining within one pixel, which, along with timing resolution, is important for resolving neutron interactions occurring in several pixels within close succession. The degree to which gamma and neutron interactions are separable using PSD was also evaluated. Based on the results of this study, we are constructing an array of pixelated organic neutron detectors based on organic glass scintillators (OGS) [9] and read out by the ARRAYJ-60035-64P-PCB.

The system is designed to perform neutron radiography and computed tomography (CT) measurements using 14.1 MeV neutrons from a deuterium-tritium (d-t) neutron generator as an active particle source. In order to reduce backgrounds from gamma activation and room scatter, the system is tagged using the Associated Particle Imaging (API) technique in which the alpha particle in the final state of the d-t interaction is used to tag both the direction and time of the neutron emission. Both the pixelated detection plane and the alpha-scintillator screen on the API d-t neutron generator are read out using the TOFPET2 ASIC and readout system developed by PETsys Electronics. The TOFPET2 ASIC is a 64-channel readout chip providing pulse time and charge integration measurements from SiPMs, and is designed for time-of-flight positron-emission tomography. The current version of the ASIC has been optimized for 3x3 mm^2 Hamamatsu (S13361-3050AE-08) or KeTeK (PA3325-WB-B0-A0-0808) SiPMs. Two ASICs are incorporated in PETsys Electronics' Front End Module (FEM), allowing for read out of 128 channels of two 8x8 arrays of SiPMs. Prior studies attempting to enable a PSD capability demonstrated some neutron/gamma discrimination [10], but due to the excellent timing properties of the ASIC [11], we rely here on time-of-flight from the alpha tag to distinguish between neutron and gamma interactions in the detection plane.

In this work we report on the predicted imaging performance of this array using Geant4: the details of the Geant4 application, imaging algorithm, and predicted performance are presented in

Section 2. Full waveform characterization of 14 pixelated OGS detectors is presented in Section 3, and includes energy and PSD performance. A description of the system, along with system level performance for a 2x2 array is included in Section 4.

2. PREDICTED IMAGING RESPONSE

We have developed a Geant4 application [12] of our system to both confirm the functionality of our imaging algorithm as well as to bound the imaging resolution and understand the optimal detector threshold for transmission imaging. Future work studying the impact of scattering within the array may also utilize the application. In this section, we describe the particulars of the Geant4 application, including the primary generator, geometry description, and output. The imaging algorithm and resulting performance are also presented.

2.1. Geant4 Simulation

The application uses Geant4 version 11.01 with the QGSP_BERT_HP physics list. The primary neutron particle energy is determined by the orientation of the generator and the neutron's trajectory, as determined by the two-body scatter interaction of the deuteron and triton:

$$\sqrt{E} = \frac{-b + \sqrt{b^2 - 4ac}}{2a} \tag{2.1}$$

with

$$a = \frac{m_\alpha + m_n}{2} \tag{2.2}$$

$$b = \sqrt{m_d m_n E_d}\cos\theta \tag{2.3}$$

$$c = \frac{-m_\alpha Q + E_d(m_\alpha - m_d)}{2}. \tag{2.4}$$

The angle between the generator's orientation and the neutron emission trajectory is θ, and m_n, m_d and m_α are the mass of the neutron, deuteron, and alpha particle, respectively. E_d is the energy of the deuteron, which is dependent on the operating parameters of the tube. Finally, Q is the energy released in the interaction, 17.590 MeV. The neutron trajectory is sampled isotropically in a solid angle restricted to a range fully covering the detector array, which in our configuration is a cone with a 15 degree opening angle. The solid angle fraction is

$$f_s = \frac{\Omega}{4\pi} = \frac{2\pi(1-\cos\phi)}{4\pi} = \frac{1-\cos\phi}{2}, \tag{2.5}$$

where ϕ is half of the cone's opening angle. The total simulated time t for N sampled neutrons and a neutron generator rate in 4π of R is:

$$t = \frac{N}{Rf_s} = \frac{2N}{R(1-\cos\phi)}. \tag{2.6}$$

The system geometry is constructed such that the target to be imaged is placed at the center. The detector plane is offset from the target in the z-dimension such that the face of the detectors is at 60 cm, and the neutron generator is at (-)30 cm in the z direction. In this configuration, the image space is magnified by 3x at the image (detection) plane, therefore we expect an imaging resolution of at most 2 mm since the detector pixels are $\sim$ 6 mm. For CT measurements, the detector, generator, and neutron emission angle are all rotated by a specified angle, and the target remains stationary. All targets are constructed of high-density polyethylene (HDPE), and the detectors are constructed of an organic scintillator material with a 1.15 g/cm^3 density and a 12:14 hydrogen:carbon fraction. Detector pixels 6.13x6.13x30 mm^3 in size are laid out in a (x,y) grid, in which pixels have a 0.2 mm gap in x and y directions to account for the SiPM pixel pitch, and every 8th pixel has a 2 mm gap to account for gaps between the detector modules. The material between gaps is air. Figure 2-1 shows a rendering of a 5x5 detector plane.

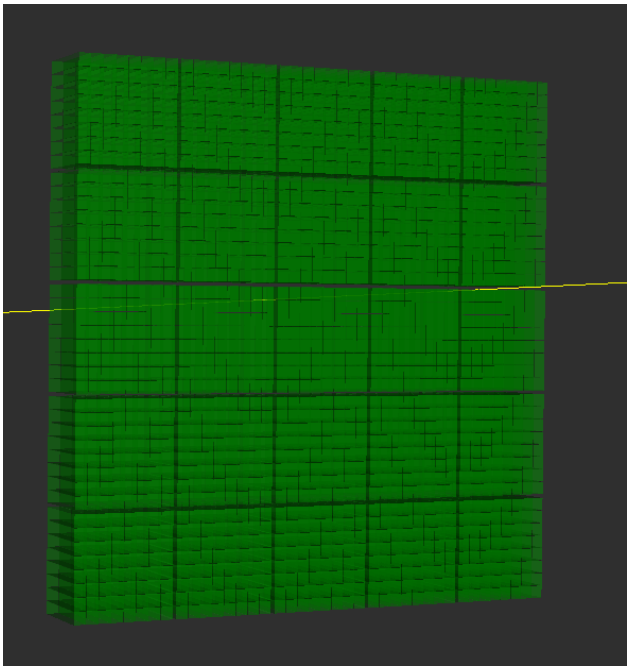

Figure 2-1. A rendering of the detector plane from the Geant4 application, with a 5x5 array of 8x8 pixels, each 6.13x6.13x30 mm^3 in size with a 0.2 mm gap between detector pixels and a 2 mm gap between detectors.

All proton recoil track information with an ionization parent process is saved for further analysis, which is based on the sum of all proton recoil energy depositions within a pixel. Depending on the pixel energy threshold, the number of interactions for each pixel resulting from both an empty (no imaging target) and full target dataset are input into the imaging analysis. Finally, it should be noted that, although the particulars of the API tagging are not modeled, we are inherently modeling the basic effect of alpha tagging due to our event generation. We do not currently model backgrounds such as activation or room return: the expectation is that these will be fully

accounted for with an empty target scan with experimental data. Future improvements could include resolving multiple scattering within single detectors, however for our current purposes this was not deemed necessary.

2.2. Imaging Algorithm and System Response

The imaging algorithm employed for this work is the Parabolical Surrogate Coordinate Decent (PSCD) [13], in which a quadratic surrogate function is used at each iterative minimization step in place of a penalized Poisson likelihood function. The critical input to the algorithm is a system map of path lengths though all possible image voxels as a function of an observation vector, in this case defined by a pixel, detector, and rotation index. Thus for a particular observation of detector hits (pixel, detector index) for a set of rotation angles, the algorithm outputs the linear attenuation coefficient of each voxel consistent with a minimization of the surrogate likelihood function.

To build a system map, we use the TGeoManager class in CERN's ROOT Toolkit [14] to construct the same geometry as defined in our Geant4 application. We then randomly sample positions within each scintillator pixel and back track a trajectory from the neutron generator location to that position within the scintillator to determine the path length through each voxel of the image space. The contribution is weighted by the probability of the interaction for that position in the scintillator based on neutron attenuation. The path length for 1000 sampled scintillator positions in each pixel is averaged. For the results presented here, the image space voxels are 2x2x2 mm^3, spanning a range of ± 4 cm in each dimension. A rendering of the geometry is shown in Figure 2-2.

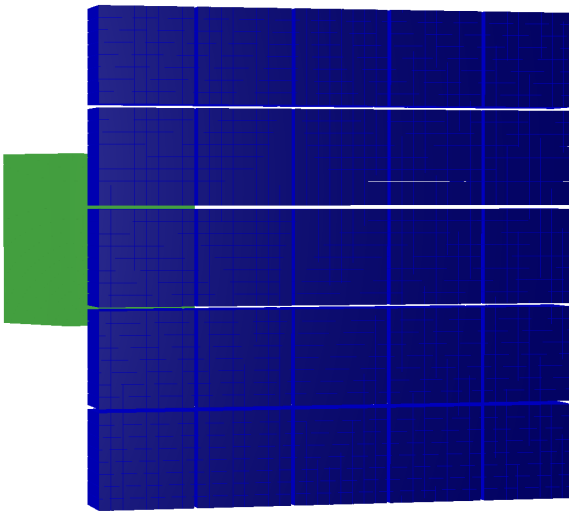

Figure 2-2. A rendering of the detector plane from the TGeoManager construction, with a 5x5 array of 8x8 pixels, each 6.13x6.13x30 mm^3 in size with a 0.2 mm gap between detector pixels and a 2 mm gap between detectors.

2.3. Results

Using the Geant4 application, we created three datasets with which to test the imaging algorithm and estimate the imaging resolution: we modeled an empty dataset with no target present, a 3x3x3 cm^3 HDPE block to estimate the imaging resolution, and a 3 cm thick HDPE Sandia thunderbird target as a complex shape demonstration. For the target datasets, seven rotation angles were simulated at 30 degree increments from zero to 180 degrees. For the empty target, we modeled $22x10^7$ primary neutrons, for a total of 514 seconds generator of runtime operating at $1x10^8$ n/s, and for each of the two targets we modeled $5x10^7$ primary neutrons, or 116 seconds generator runtime for each rotation. Each target was evaluated for total detector energy deposition thresholds of 2, 5, 8 and 10 MeV.

Figure 2-3 shows the number of entries for each of the 4 energy thresholds for the empty and block target datasets as a function of the observation bin, in this case the detector pixel number, rotation angle index, and detector number, in that order. The difference in number of counts from (0,56), (0,488) and (0,2240) in the empty dataset are a function of the pixel's location within each detector and within the detector array itself, and presumably due to scattering within the array or perhaps attenuation within the detector array: these features become less pronounced for higher threshold energies.

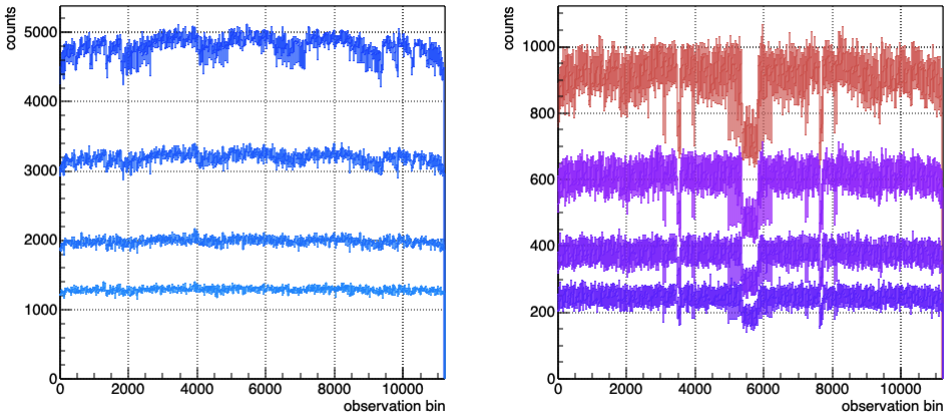

Figure 2-3. The number of entries for each of the 4 energy thresholds for the empty (left) and block target (right) datasets as a function of the observation bin, or the pixel, rotation and detector index.

Figures 2-4 and 2-5 show the reconstructed images in 3 and 2 dimensions for the 3x3x3 cm^3 block target for all four energy thresholds, and confirm that the algorithm and system map construction are functional. The minor imaging artifacts that become more prevalent with increasing energy threshold are presumably due to lower statistics at those energies in both the target and empty datasets: the average number of entries for the target dataset drops from 901 to 240 and from 4795 to 1285 for the empty dataset. The derivative of the 2D images are fit to a Gaussian to determine the imaging resolution (Figure 2-6), which for the artifact-free projection (x) ranges from 0.6 to 3 mm depending on the energy threshold.

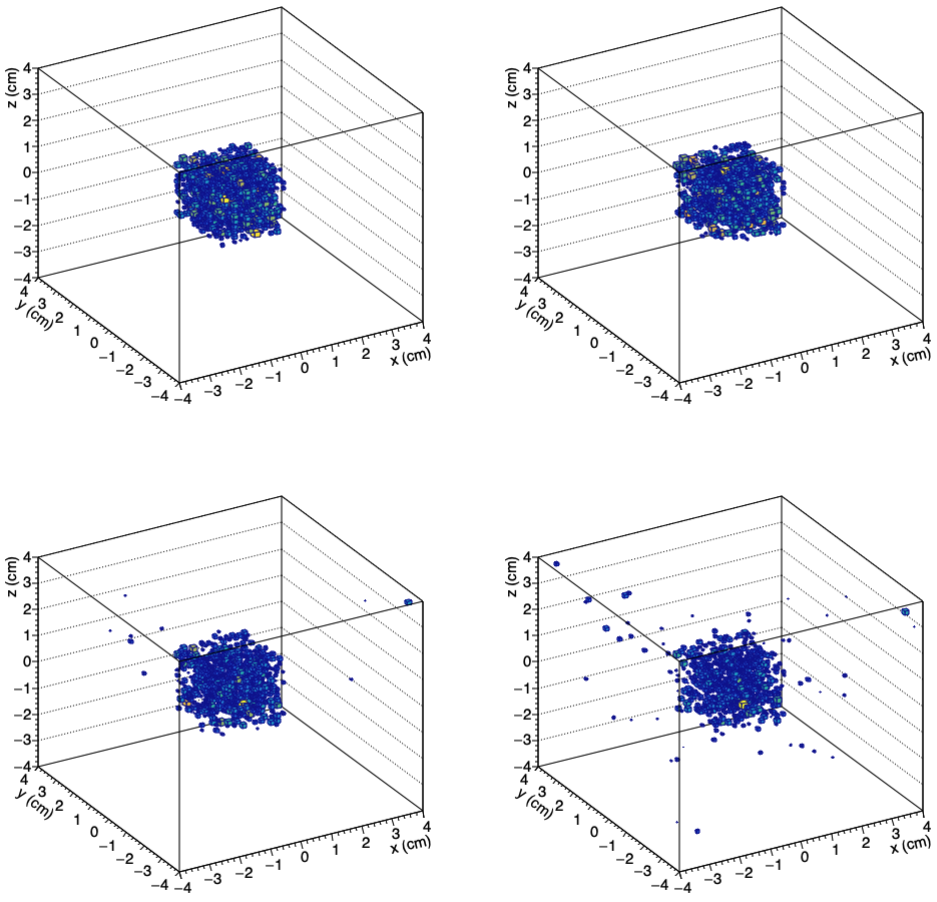

Figure 2-4. The 3D image reconstruction of the 3x3x3 cm^3 block target for (from top, left) 2, 5, 8 and 10 MeV energy thresholds.

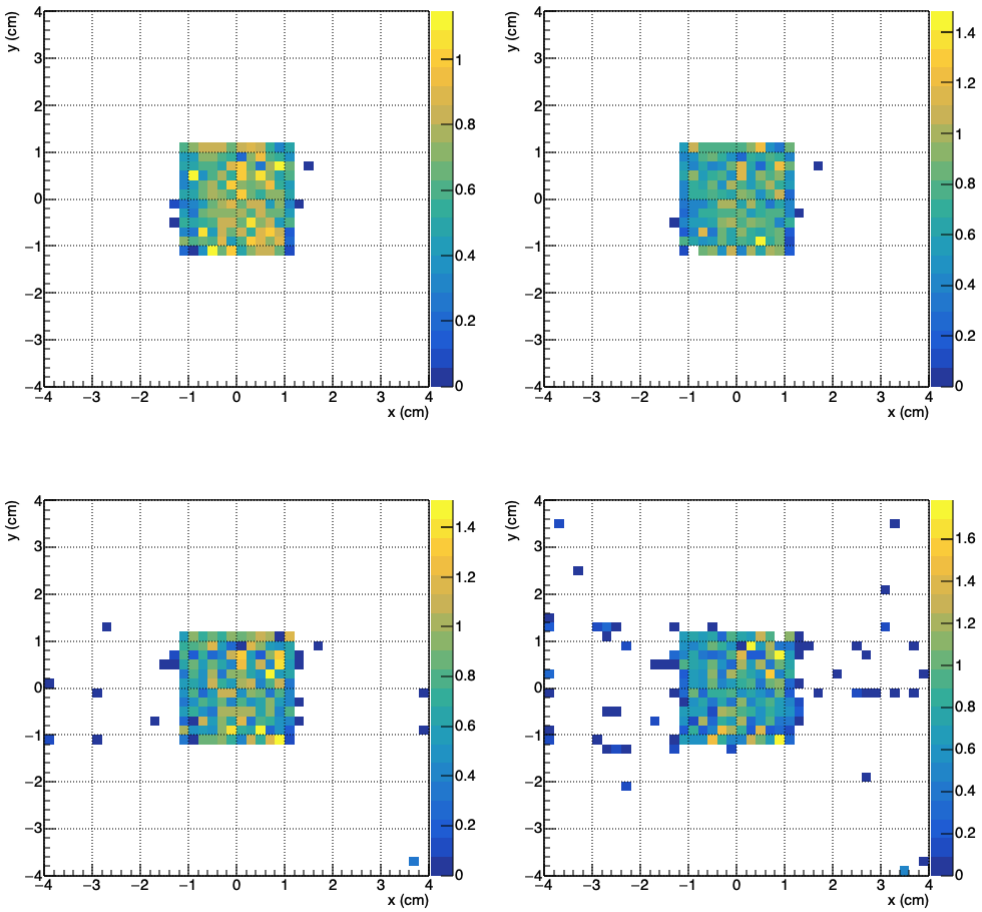

Figure 2-5. The 2D (x,y) image reconstruction of the 3x3x3 cm^3 block target for (from top, left) 2, 5, 8 and 10 MeV energy thresholds.

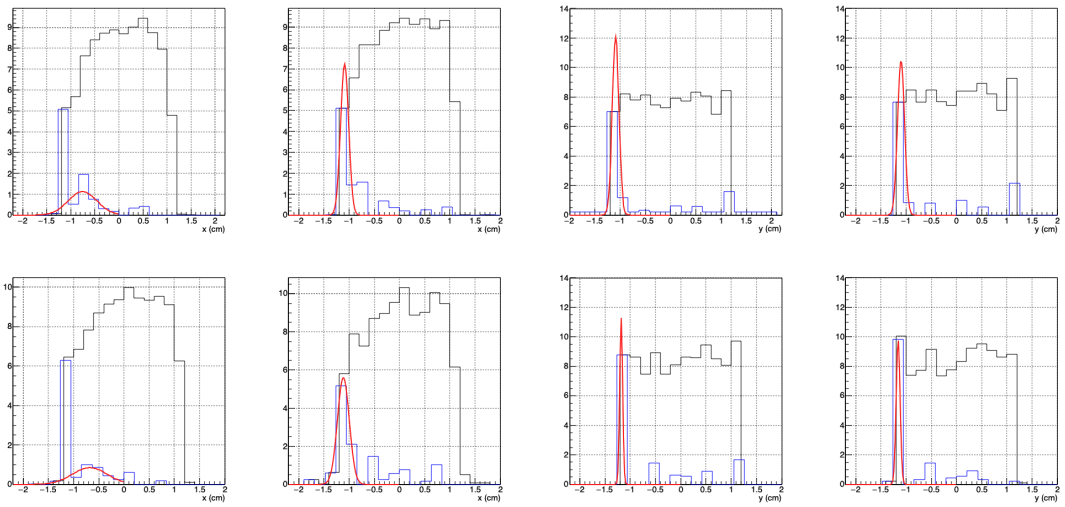

Figure 2-6. The x and y projections of the 2D image reconstruction of the 3x3x3 cm^3 block target for the four energy thresholds. The derivative of the projection is fit with a Gaussian to measure the imaging resolution.

The observation bin counts and 3D and 2D image reconstruction for the thunderbird target are shown in Figures 2-7 through 2-9, and demonstrate the image reconstruction for a more complex target. As seen before, image artifacts increase with energy threshold, again presumably due to limited statistics.

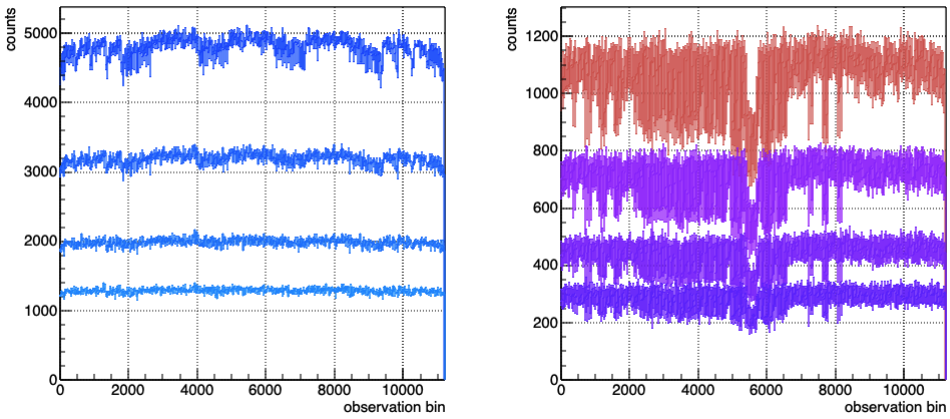

Figure 2-7. The number of entries for each of the 4 energy thresholds for the empty (left) and thunderbird target (right) datasets as a function of the observation bin, or the pixel, rotation and detector index.

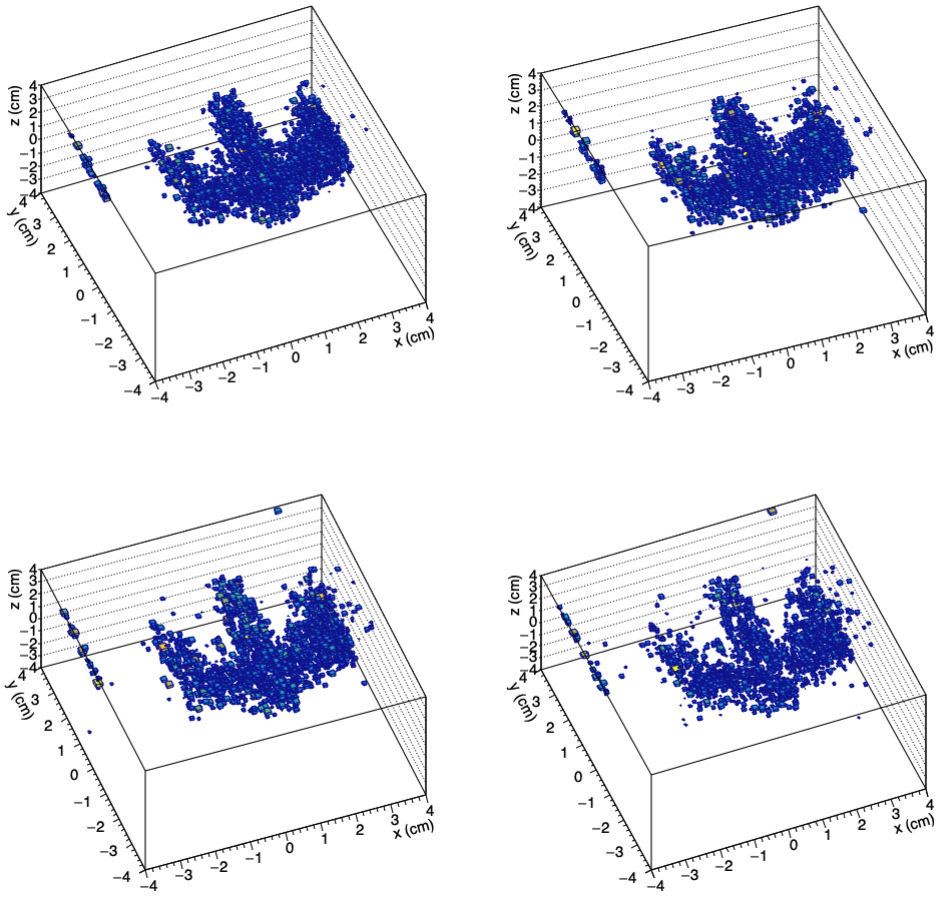

Figure 2-8. The 3D image reconstruction of the 3 cm thick thunderbird target for (from top, left) 2, 5, 8 and 10 MeV energy thresholds.

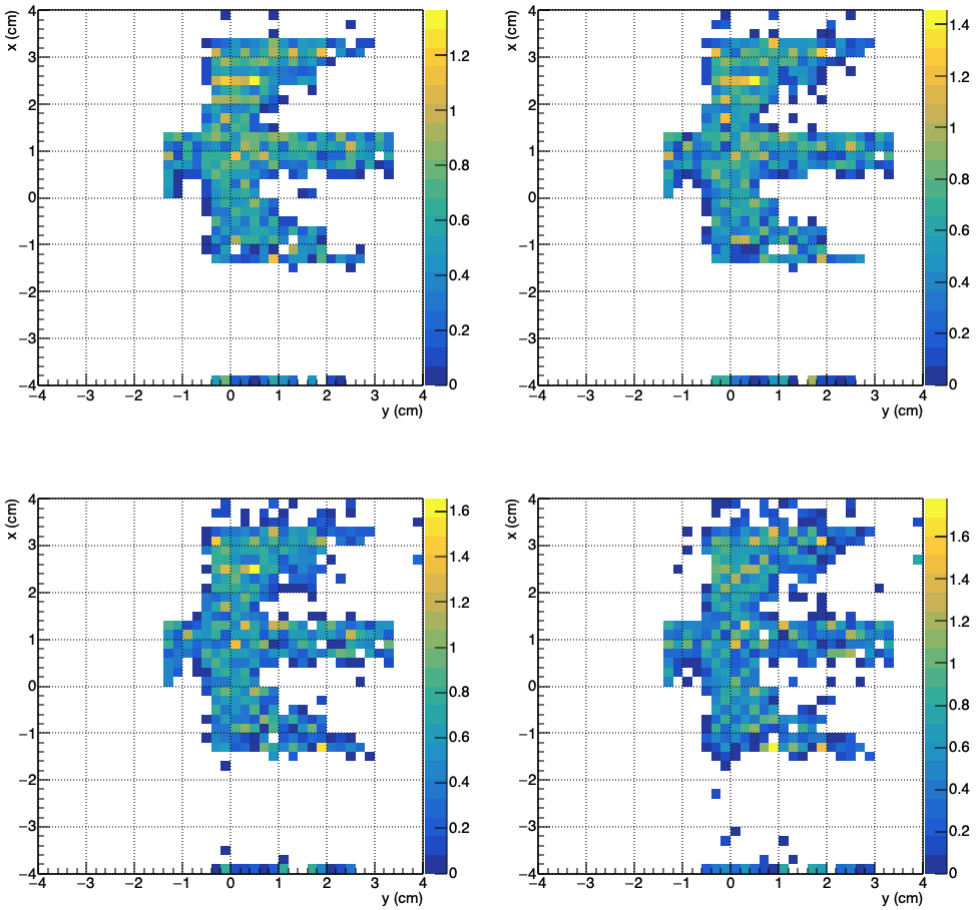

Figure 2-9. The 2D (x,y) image reconstruction of the 3 cm thick thunderbird target for (from top, left) 2, 5, 8 and 10 MeV energy thresholds.

3. DETECTOR CHARACTERIZATION

We previously reported on the performance of several different pixelated detectors [8]. Based on the results of that study, we have constructed 14 organic glass-based pixelated detectors. There have been minor changes to the formulation to allow for a design without outer fins so that the detectors can be close-packed. Figure 3-1 shows an array with outer fins from the prior characterizations compared to a fin-less detector from the current batch.

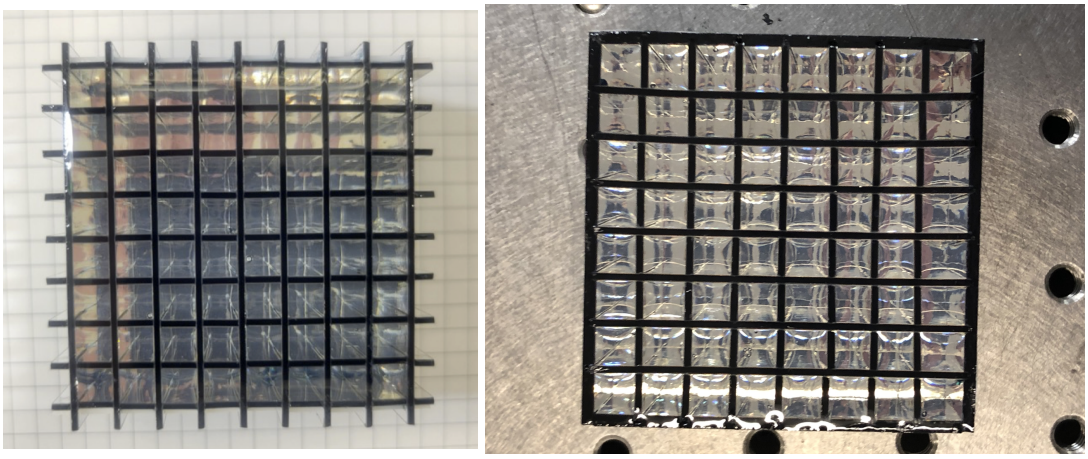

(a) (b)

Figure 3-1. A detector with fins from the prior characterization (a) and a fin-less design from the current batch of detectors (b, Array AIB-6-87).

Each detector in the array is characterized individually in terms of its overall light collection uniformity and PSD performance. The detectors are coupled with silicone optical grease to an ArrayJ-60035-64P-PCB SiPM, which is mated to a custom 64 channel breakout board, shown in Figure 3-2a [15]. The board is biased at (-)30 V with a B&K Precision 1761 DC power supply. All measurements were conducted in a temperature-controlled laboratory where the maximum allowed temperature range varies in the range 65-75°F, or 18.3-23.9°C: typically the temperature swings are not this extreme. According to the product datasheet, the temperature coefficient of the breakdown voltage is 21.5mV/°C. The breakdown voltage (V_{bd}) for each device is 24.2-24.7 V (or 24.45±0.25) at 20°C. Based on these numbers, we expect a maximum bias (V_{bias}) change of:

$$V_{bias}(T) = V_{ov} + V_{bd} \tag{3.1}$$

$$= V_{ov} + 24.45 + 0.0215(T - 20). \tag{3.2}$$

This results in a range of $24.4 \leq V_{bias} \leq 24.5$, which is less than the quoted precision on the breakdown voltage but will induce a small gain variation in the datasets. Again referring to the

product's datasheet, the typical gain dependence is 1e6/V. This is an approximate 1-5% effect at the over-voltage that we are operating them at. It should also be noted that, due to the low light output of organic scintillators, saturation effects due to micro-cell dead time are not expected to impact the results presented here.

The SOUT of the SiPM pixels are read out in groups of 16 with header pins that mate to CAEN's A385 adaptor with MCX connectors. The assembly is in a light tight enclosure. The data acquisition electronics are shown in Figure 3-2b: four 16 channel CAEN 725 digitizers acquire the SOUT channels with 250 MHz, 14-bit digitization.

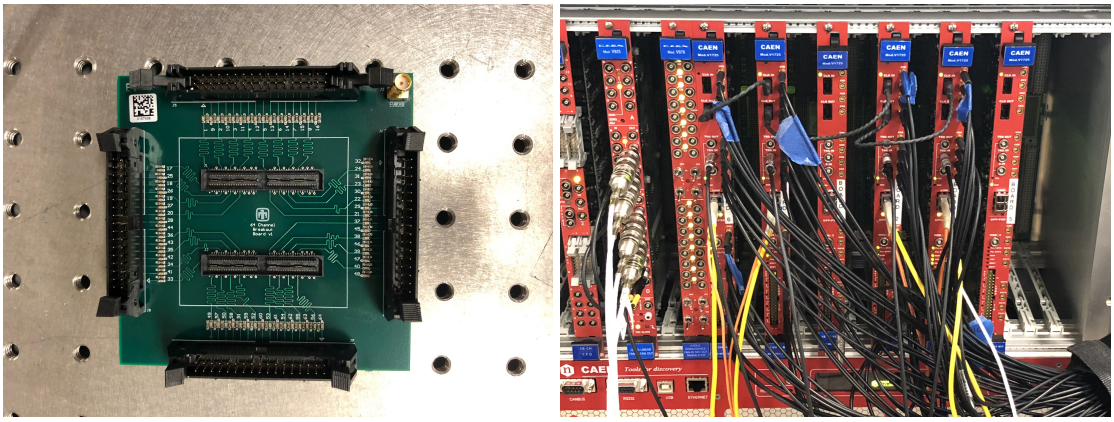

(a) (b)

Figure 3-2. The readout electronics for comparison measurements with full digitization. (a) The 64-channel SOUT break out board and (b) several 16-channel 725 digitizers from CAEN.

All analysis operations are written in C++, utilizing algorithms from the ROOT analysis toolkit [14]. Before energy and PSD characterizations, the waveforms are baseline subtracted using the first 80 ns of the trace and a centered moving average filter is applied. The cumulative distribution of the waveform is used to calculate the pulse integral for total energy deposition measurements. Due to a pulse height dependent undershoot, the integral is evaluated 280 ns after the pulse time by interpolating the cumulative distribution of the waveform between samples. The pulse time is the linearly interpolated value between waveform samples corresponding to 50% of the maximum value on the rising edge. For pulse shape measurements, we linearly interpolate between samples of the cumulative distribution of the waveform for the value corresponding to the desired integration window.

3.1. Light collection and energy response

The calibration from pulse integral to MeVee is determined by fitting the measured spectrum to a smeared Klein–Nishina spectrum from a ^{137}Cs source [16]. The method outlined is similar to that presented in [17, 18]. The pulse integral spectrum from the ^{137}Cs source is used to compare to the expected spectrum calculated from the Klein–Nishina prediction. First, the experimental result is converted to MeVee units with a linear transformation:

$$E_{keVee} = q_0 E_{mV} + q_1. \tag{3.3}$$

Next, an arbitrary y-scale, q_2, is applied to the Klein-Nishina prediction for the gamma emissions, and a Gaussian convolution is performed with a standard deviation of:

$$\frac{\sigma}{E_{MeVee}} = \sqrt{q_3^2 + \frac{q_4^2}{E_{MeVee}} + \frac{q_5^2}{E_{MeVee}^2}}. \tag{3.4}$$

For successful fitting, some parameters are fixed, and the fit region is restricted to a range near the Compton edge. In this case, the primary parameter of interest is the conversion factor to MeVee. Figure 3-3 shows an example fit for one pixel.

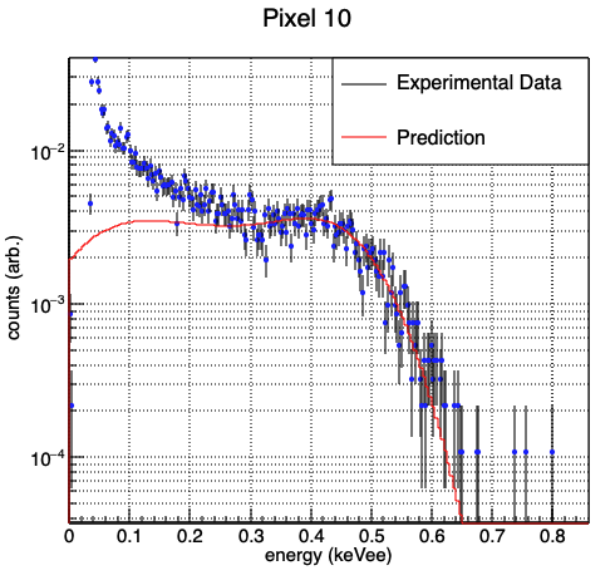

Figure 3-3. An example Compton edge fit, with the smeared Klein-Nishina spectrum from ^{137}Cs shown in red, and the experimental data in blue.

In order to evaluate the light collection, the raw pulse height value corresponding to 340 keVee is reported for each array: this is done for comparison to prior results that used a ^{22}Na source for energy calibrations. Figure 3-4 shows the calibrated energy spectrum as a function of pixel number for all 64 pixels in array AIB-6-95, and the energy as a function of pulse height for all pixels. From these two plots, one can determine both the quality of the energy calibration for all pixels as well as the light collection uniformity. The reported light collection is the projected pulse height in the 335-345 keVee bin for all 64 pixels, shown in Figure 3-4c. For this example, the reported light collection is 125±14: the error reported is the standard deviation of the projected distribution.

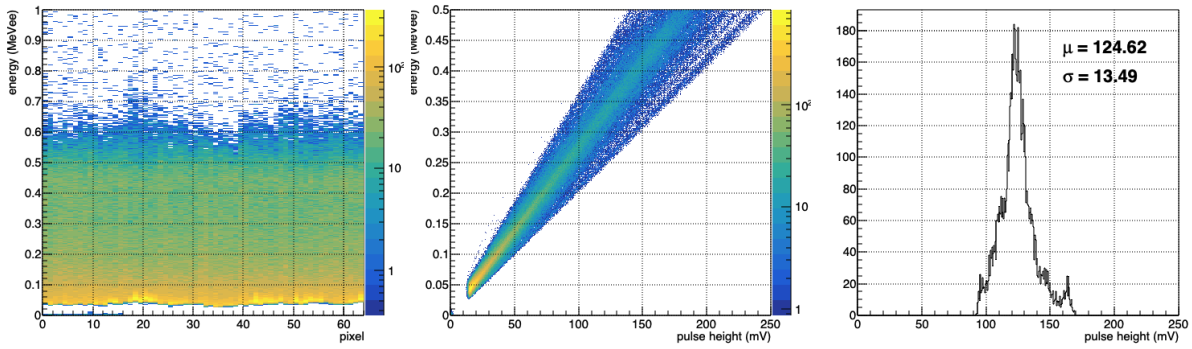

(a) (b) (c)

Figure 3-4. The calibrated energy spectrum for all pixels in AIB-6-95 is shown in (a). The calibrated energy as a function of pulse height for all pixels is shown in (b). The pulse height projection for all pixels in the array in the calibrated 335-345 keVee energy range is shown in (c): the light collection for this array is reported as 125±14.

3.2. Pulse Shape Discrimination

The pulse-shape parameter used in this report is defined as the ratio of the tail pulse integral to the total pulse integral. The start time of the tail region is determined by optimizing the figure-of-merit, defined as

$$FoM = \frac{\mu_n - \mu_\gamma}{2.355(\sigma_n + \sigma_\gamma)}, \tag{3.5}$$

where $\mu_{n/\gamma}$ is the mean of a Gaussian fit to the neutron and gamma distributions, $\sigma_{n/\gamma}$ is the standard deviation of the Gaussian fit, and the factor of 2.355 is for conversion to a FWHM width. The shape of the fission neutron energy spectrum favors optimizing the FoM for lower energy depositions in order to maximize overall neutron detection efficiency. For this reason we start the tail integration at 40 ns, which was consistently the best overall value for all arrays: at this value and for each array, the FoM for 50 keVee is maximized. The optimized energy-dependent FoM for all pixels in array AIB-6-95 is shown in Figure 3-5. For each array, we report the mean and standard deviation for all pixels in an an array at 340 keVee: for this array we report a FoM of 1.29±0.21.

3.3. Results

The characterization results for 14 detectors is reported in Table 3-1. The first entry (20210607) is for the finned design previously reported on, included here for comparison purposes. The results are further grouped into two, separated in the table by a horizontal line, to indicate slight changes to the scintillator formulation and casting process to improve overall robustness of the arrays. The majority of the results are either within 10% of the finned design, or have improved performance. Arrays AIB-6-87 and AIB-6-97 have a 14% increase in PSD FoM compared to array 20210607.

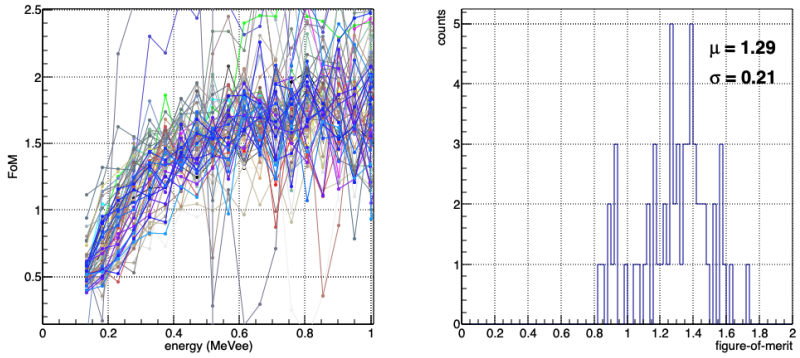

(a) (b)

Figure 3-5. (a) The PSD FoM of AIB-6-95 for a 40 ns tail start time, as a function of deposited energy for all 64 pixels of the array. (b) The projected FoM values at 340 keVee for all pixels in the array, with a mean and standard deviation of 1.29±0.21.

Arrays AIB-6-89, AIB-6-94, and AIB-6-106-C show greater than 10% reduction in performance in either light collection or PSD FoM, with AIB-6-106-A showing a 38% reduction in PSD FoM. The cause of such a large difference in performance is under investigation. The first four entries, indicated in bold, areincluded in the 2x2 detector array. The position of each detector in the 2x2 array is indicated by (BR/BL) for bottom-right/left and (TR/TL) for top-left/right.

Array	Light Output (mV)	PSD *FoM*
20210607	126±9	1.25±0.19
AIB-6-87(BR)	134±11	1.42±0.18
AIB-6-88(BL)	134±13	1.38±0.19
AIB-6-89(TR)	109±24	1.06±0.25
AIB-6-90(TL)	118±21	1.20±0.27
AIB-6-94	114±12	0.96±0.20
AIB-6-95	125±14	1.30±0.20
AIB-6-96	123±12	1.16±0.29
AIB-6-97	134±13	1.42±0.16
AIB-6-98	126±17	1.21±0.29
AIB-6-102	127±11	1.24±0.17
AIB-6-103	123±9	1.27±0.13
AIB-6-103-C	119±8	1.05±0.24
AIB-6-106-A	110±7	0.77±0.12
AIB-6-106-B	127±17	1.15±0.26

Table 3-1. Light output and PSD *FoM* results at 340 keVee for all arrays. Entry 20210607 is the result from prior work.

4. SYSTEM RESPONSE

The complete system response is presented for a 2x2 array of organic glass pixelated detectors read out with the TOFPET2 readout system. Below we describe the experimental setup, TOFPET2 readout system, timing characterizations, and response to d-t API neutron generator emissions.

4.1. Experimental Setup

The detectors included in the 2x2 system are shown in Figure 4-1, and the detectors inside the mechanical assembly is shown in Figure 4-2. Plastic shim material ranging from 0.010-0.025" is used to align and square the scintillator arrays within the enclosure wall, which for this prototype assembly is 3D printed (shown in Figure 4-2). The detector assembly is attached with screws to the SiPM assembly, shown in Figure 4-2b, in which silicone foam walls surround each SiPM array. A second layer of foam sits behind each SiPM array to account for slight differences in detector length. Silicon optical grease is used for optical coupling. The entire assembly is mounted on a cart with a breadboard for precise positioning relative to the d-t API neutron generator.

For measurements with the d-t API neutron generator, the detector array is positioned 30 cm from the target region, and the generator is positioned 30 cm from the target region in the opposite direction. These preliminary characterizations differ from the simulation: future imaging runs will use the configuration from the simulation. Figure 4-5 shows a graphic representation of the measurement setup. At these distances, each 0.3 cm pixel on the d-t tube alpha screen SiPM corresponds to a 3 cm distance on the OGS detection plane (or, alternatively, 5 J-series pixels). One pixel of the OGS array corresponds to a feature size of 0.3 cm of the target object. The feature size of the target object can be reduced by moving the 2x2 array organic glass pixelated detectors to farther distances from the target at the cost of lower count rates. The target area rotates to allow for images of the object at various angles.

The API neutron generator is operated at 50 μA and 60 kV for all measurements. Neutrons from the generator are tagged by an associated alpha particle that is coincident in time and traveling in the opposite direction. An alpha scintillator screen on the neutron generator is read out with a Hamamatsu S13361-3050AE-08 array that is integrated into the TOFPET2 readout system, allowing for coincident readout of both the alpha screen and detector array, which are read out by SensL/Onsemi's ARRAYJ-60035-64P-PCB. A depiction of the complete setup is shown in Figure 4-4. The setup includes the 2x2 OGS pixelated array, a TOFPET FEB/D board, a TOFPET Clock&Trigger board to sync times across FEB/D boards, five FEMs, ASIC cooling fans, and a data acquisition computer. The total channel count of the system is 320. Figure 4-3 shows the

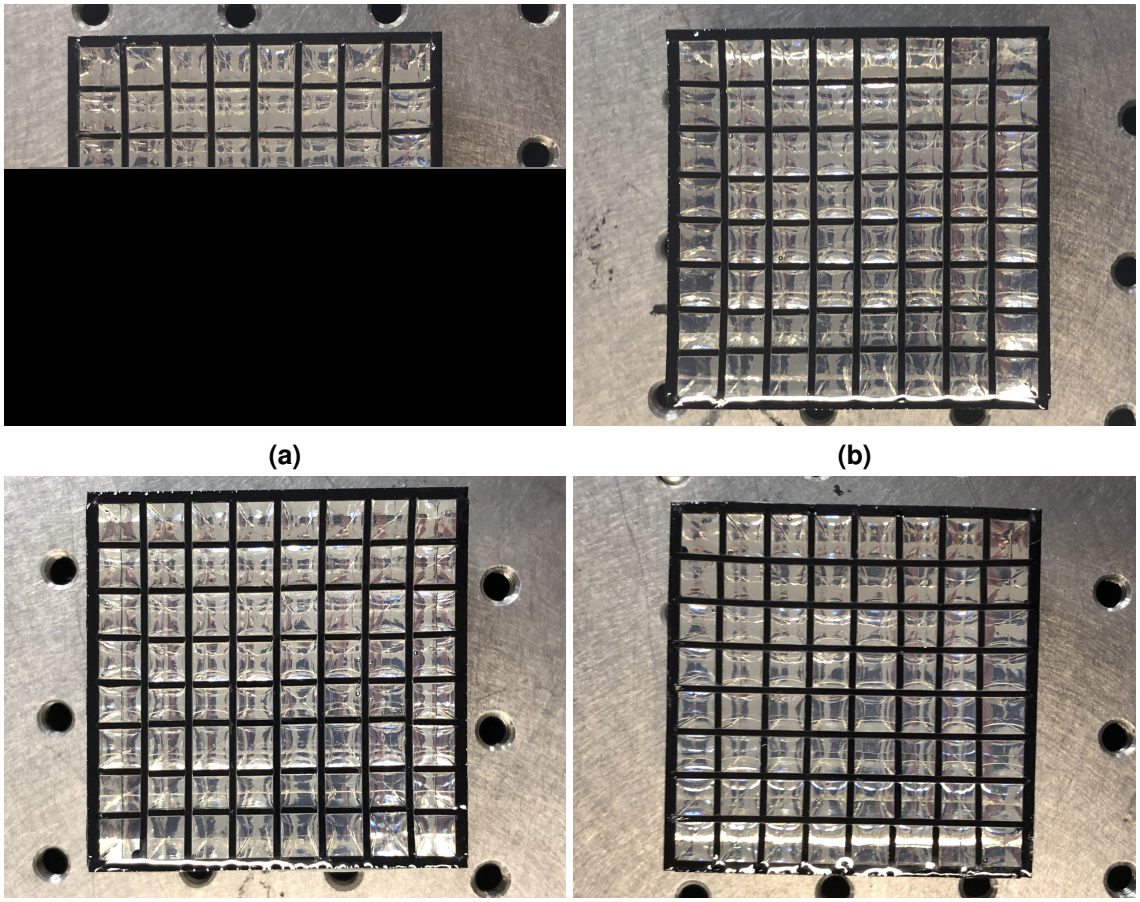

(a) (b)

(c) (d)

Figure 4-1. The front face of the four detectors used in the 2x2 array. From the top, left: AIB-6-90 (a), AIB-6-89 (b), AIB-6-88 (c), and AIB-6-87 (d).

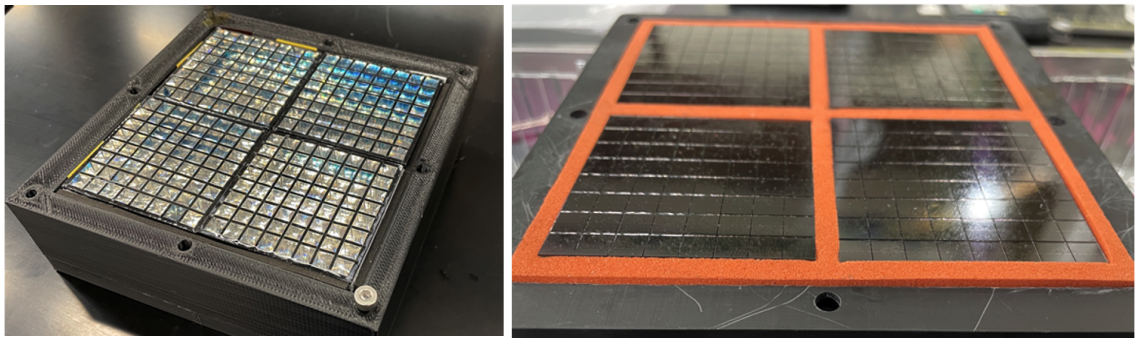

(a) (b)

Figure 4-2. A prototype of the mechanical array of scintillators and SiPM boards. (a) The lower assembly: Plastic shim material ranging from 0.010-0.025" is used to align and square the scintillator arrays within the enclosure wall. (b) Upper assembly: Silicone foam walls surround each SiPM array. A second layer of foam sits behind each SiPM array to take up any differences in length of the detector arrays.

Hamamatsu S13361-3050AE-08 array coupled to the alpha screen (also shown on the top of Figure 4-4).

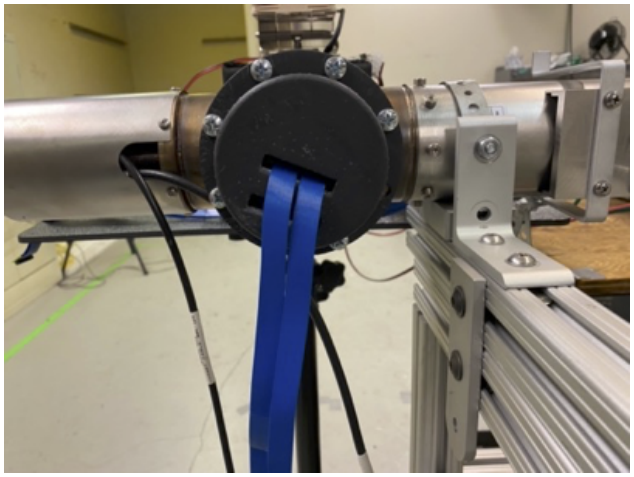

Figure 4-3. The d-t tube, with the alpha screen read out by Hamamatsu S13361-3050AE-08 array coupled to a FEM, within a light tight enclosure.

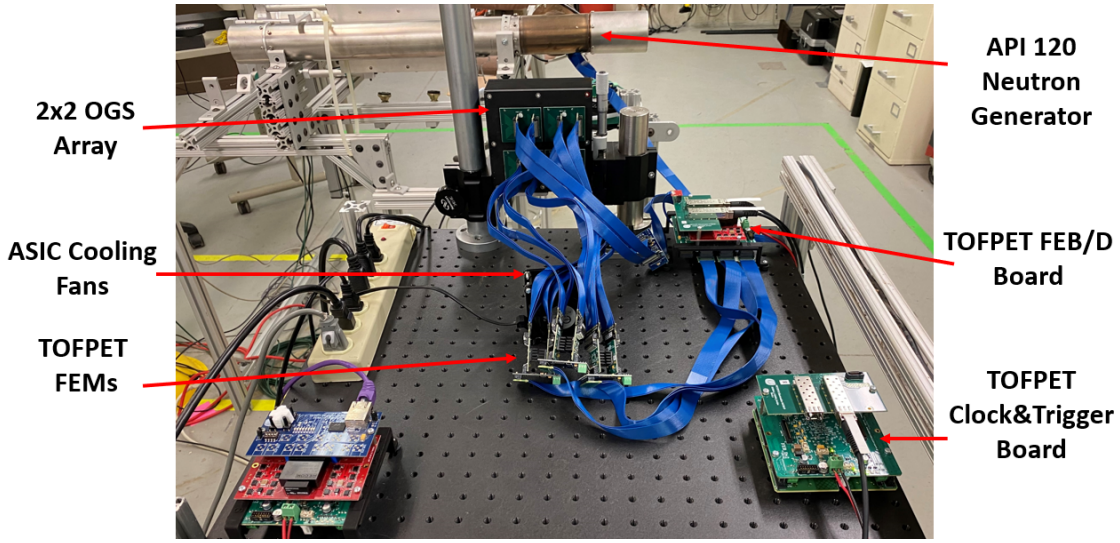

Figure 4-4. TOFPET2 Readout system setup with the API 120 neutron generator. Experimental setup for the 2x2 OGS array includes a TOFPET FEB/D board, a TOFPET Clock&Trigger board to sync times across FEB/D boards, five FEMs, ASIC cooling fans, and a data acquisition computer (not shown).

4.2. Readout System

All SiPMs are read out using the TOFPET2 readout system from PETsys Technologies, which is built around an ASIC that provides 64 channels of charge integration and pulse timing measurements. The front-end-module (FEM) consists of a SiPM interface board, two ASIC chips, and a board that interfaces with the readout module. One readout module (FEB/D), which consists

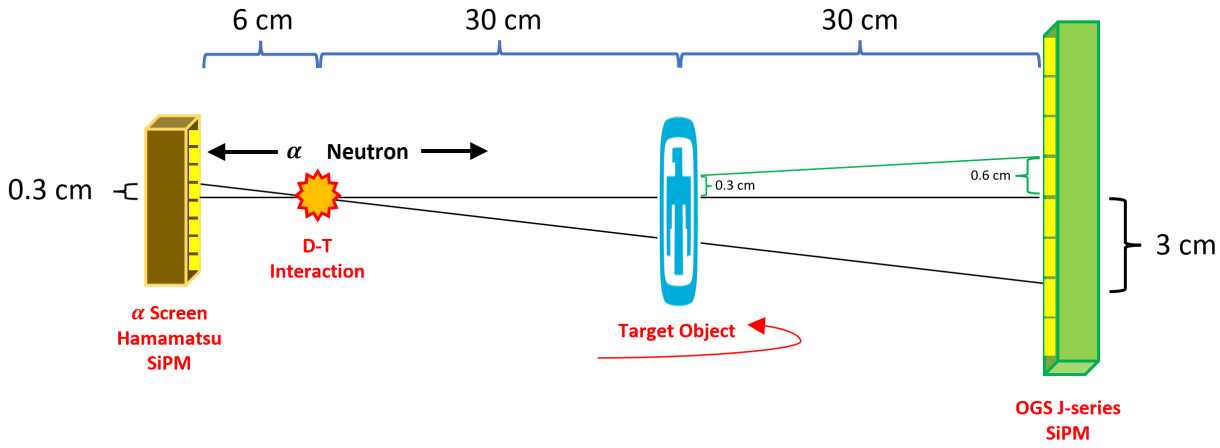

Figure 4-5. Graphic representation of the measurement setup (not to scale).

of SiPM bias, computer communication, and FPGA boards, can interface with up to 8 FEMs. Individual readout modules can be integrated into one system for thousands of readout channels. PETsys Technologies has designed a custom SiPM interface board for SensL's ArrayJ-60035 64P-PCB that splits the output of each SiPM and routes them to two adjacent ASIC channels, allowing for two charge integration measurements with configurable integration time window lengths. This enables the 64 SiPMs to be read out by the 128 channels of the TOFPET2 FEM. Figure 4-6 shows the FEM with the custom SiPM interface board, coupled to the J-series array.

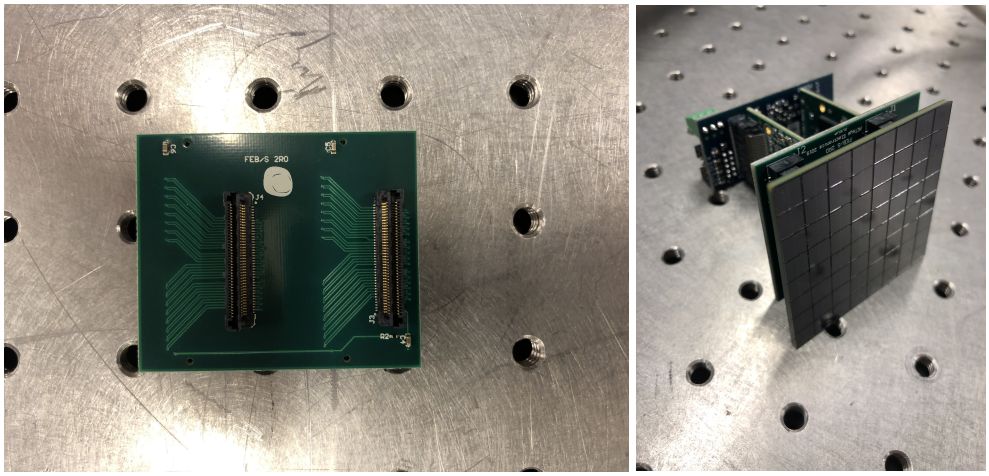

(a) (b)

Figure 4-6. The custom SiPM board (a) for coupling SensL's ArrayJ-60035 64P-PCB to the front-end module (FEM), shown here assembled with the SiPM array (b).

The pre-amplifier stage of the ASIC is optimized for SiPMs with 320 pF total capacitance [11, 19], whereas the J-series 6x6 mm^2 SiPMs has a total capacitance of 4140 pF. Some parameters of the pre-amplifier can be adjusted by the software, nevertheless pre-amplifier performance is expected to be affected by a 13x increase in input capacitance. The ASIC implements a dual threshold trigger on the rising edge of the SiPM pulse after both the

pre-amplification stage and an additional amplifier [11, 20]. The first (T1) discriminator is set low to capture the rising edge of the pulse. To eliminate triggers on noise (SiPM dark counts) a second (T2) discriminator is set to a higher threshold. Crossing both thresholds within a given delay time applied to T1, set to account for the rise time of the pulse, triggers the system with no dead time. The timing measurement is made on the logical AND of the delayed T1 and T2 triggers, and depending on which gate is opened first, an erroneous delay added to T1 will be applied to the timing measurement, causing satellite peaks in the coincident timing distribution [20]. The thresholds on T1 and T2 must be carefully set for the particular noise level in the SiPMs to eliminate these satellite peaks.

Finally, there is a separate "E" channel with a lower post-amplification than the two "T" channels. Events that do not cross this threshold are rejected with a five clock cycle dead time. The system can work in two modes: a TOT mode in which high-precision pulse rise and fall times are used for energy measurements, and a QDC mode in which the high-precision rise time is used only for timing measurements while the energy measurement is provided by integrating the pulse with a QDC. In TOT mode, which is used for our measurements, the falling threshold is set on the "E" channel. In QDC mode, the charge measurements are performed on the output of the pre-amplification stage using a 10-bit ADC with configurable gain. The integration window begins at T1 and continues for a user-configurable number of 200 MHz clock cycles. This results in a 5 ns jitter in the integration time; however, there is also a high-precision measure of the true integration window time length event by event, allowing for corrections to be applied.

The system was set up following guidance from PETsys Electronics' TOFPET2 ASIC SiPM Readout System, Hardware User Guide (v1.5). For the 2x2 system only one FEB/D board is required, however to scale to an eventual system 4x4, three FEB/D boards will be required to read out the sixteen detector SiPMs plus the one alpha screen SiPM. Each FEB/D will be synced with a clock and trigger unit, and communication to the computer is through an optical connection to a PCI card. For the 2x2 system, communication is through Gigabit ethernet. The data acquisition computer is a Linux system running RedHat 7/8. Software is provided by PETsys Electronics for data acquisition and calibration of the ASIC components, which are applied by several C++ executables utilizing data analysis classes from the ROOT Toolkit from CERN [14]. Channel mapping from the ASIC to the SiPM pixels is input into a text-based map, informed by the layout documentation of the custom SiPM interface board from PETsys Electronics.

Before data acquisition runs, the readout system components must be calibrated at a stable temperature. The discriminator calibration determines the baseline and noise levels with a threshold scan while the SiPM bias is set to a value below the breakdown voltage. Dark count rates are determined with a threshold scan with the SiPM biased at the operational voltage. The TDC calibration consists of a series of test pulses with known phases. Finally, the QDC calibration procedure varies the integration window of series of test pulses, and determines the baseline offset to be removed. Each calibration is performed with an automatic script that takes approximately one hour to perform. The recommendation from the manufacturer is to perform the calibration and all measurements at ASIC temperatures below 50°C, and to remain stable to within 1°C during the run. If the temperature of a data run is greater than 5°C from the value at calibration, the calibration should be repeated. The system provides temperature measurements from two sensors located near each ASIC chip. Figure 4-7 shows the temperature stability of our

laboratory setup. By using adhesive heat sinks on each chip (with some exceptions) and applying cooling fans, the temperature for all ASICs in the setup remains well below 50°C, and the temperature of each chip is stable to within 1°C, as recommended.

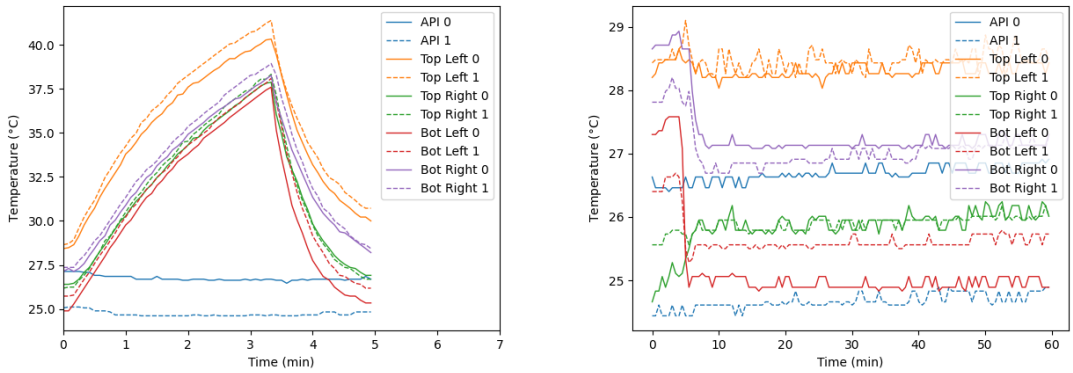

Figure 4-7. Temperature stability of the ASIC chips. (a) In this configuration, the cooling fans were turned off of all but the two API ASIC chips at 20 seconds into the measurement: the temperature increased to higher than 40°C for some chips within 3.5 minutes, after which the cooling fans were restarted. (b) Temperature stability during calibration: fans were adjusted until about 5 minutes into the measurement, after which the calibration was started. Each ASIC has an adhesive heat sink attached, aside from the two "top left" chips and the "API 0" chip.

4.2.1. Timing Calibration

As described above, to eliminate triggering on SiPM dark counts, pulses must cross both a T1 and T2 discriminator, in which T1 is typically set to a lower threshold to capture the rising edge and T2 is set to a threshold above the amplitude of the noise pulses. Crossing both thresholds within a given delay time (fe_delay) applied to T1 triggers the system with no dead time. Figure 4-8 demonstrates the nominal behavior of this triggering: the time difference between this channel and a coincident pulse on an adjacent channel will have a mean centered at $\sim$ 65 ns for this example in which fe_delay = 5 ns, since the timing measurement is made on the AND of the delayed T1 and T2 triggers. If, however, the do_T1_delayed gate is active when the main pulse crosses the T2 threshold, fe_delay will not enter into the time difference. This is demonstrated by Figure 4-9, in which T_trigger is opened at 60 ns rather than 65 ns in the nominal case. This behavior will cause satellite peaks centered at the true coincident time $\pm$fe_delay. To counteract this effect, the T1 and T2 thresholds, combined with the fe_delay time, should be calibrated such that the satellite peaks are highly suppressed or are well outside any timing features of interest. Because the T1 and T2 settings can impact timing resolutions and the relative timing offsets between channels, this optimization is performed before calibrating the ASIC channel timing offsets and characterizing the coincident timing resolutions.

As a demonstration, Figure 4-10 shows how satellite peaks manifest when plotting the timing difference between two coincident events (in this case two coincident 511 keV gammas emitted

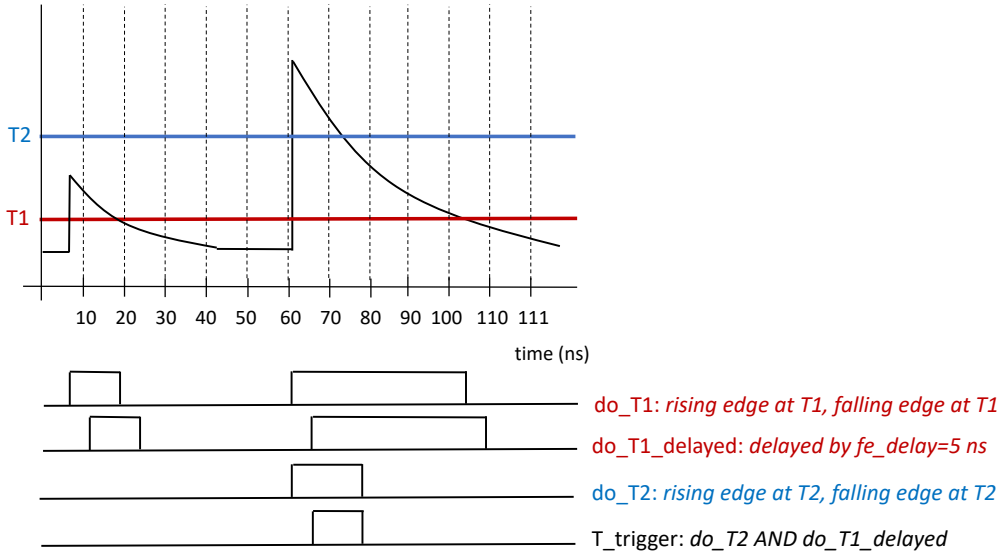

Figure 4-8. The nominal behavior of TOFPET2 ASIC triggering. In this case, the noise pulse's falling edge on the T1 discriminator is further from the main pulse than the fe_delay length, and thus do_T1_delayed is not active when the main pulse crosses the T2 threshold. The time difference between this channel and a coincident pulse on an adjacent channel will have a mean centered at $\sim$ 65 ns for this example in which fe_delay = 5 ns.

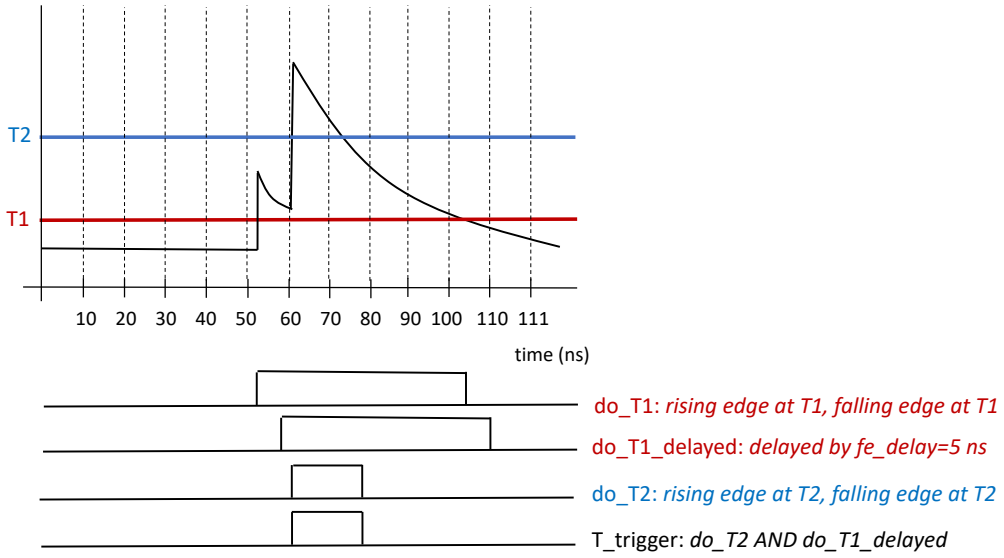

Figure 4-9. The pathological behavior of TOFPET2 ASIC triggering. In this case, the noise pulse's falling edge on the T1 discriminator does not occur before the main pulse, and thus do_T1_delayed is active when the main pulse crosses the T2 threshold. The time difference between this channel and a coincident pulse on an adjacent channel will have a mean centered at $\sim$ 60 ns for this example.

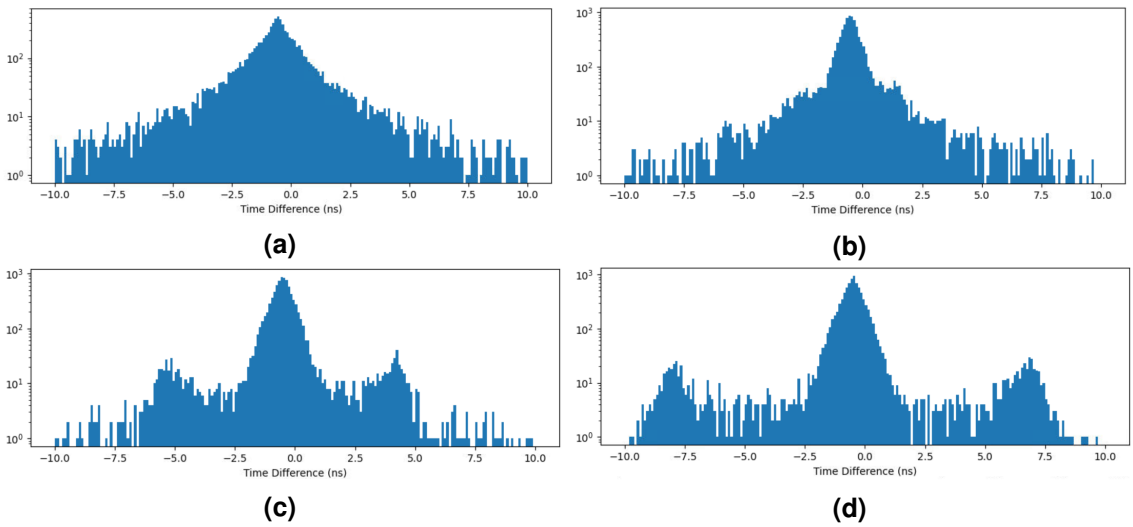

Figure 4-10. fe_delay settings that affect satellite peak positioning. Satellite peaks manifest at $\pm$fe_delay and can be seen in (c) and (d). (a) 0 ns delay (No delay). (b) 3 ns delay. (c) 6 ns delay. (d) 8 ns delay.

from a ^{22}Na source and detected by a 6 mm cube of *trans*-Stilbene). The fe_delay was set at 0 ns, 3 ns, 6 ns, and 8 ns. The satellite peaks are easily discernible at delays of 6 ns and 8 ns; however, at 3 ns and 0 ns, the satellite peaks merge with the true coincidence peak near 0.5 ns making differentiation between a true coincidence and a dark noise induced count difficult or impossible. It is important to set the fe_delay to a time that dose not interfere with the neutron/gamma flight times of interest for each particular measurement.

As stated earlier, dark counts will contribute true events to satellite peaks at a ±fe_delay timing difference. The positive or negative time shift is determined by which SiPM the dark count was detected before the true scintillation event occured; For a coincidence measurement, if the thresholds are set correctly for one SiPM and not the other, a single satellite peak will manifest at either +fe_delay or -fe_delay rather than having a double satellite peak as shown in Figure 4-10.

For the 2x2 system using the API neutron generator, the satellite peak at a positive time difference was removed by increasing both the T1 and T2 threshold for the organic glass arrays in increments of 10 units from 20 to 90 until the peak disappeared. Figure 4-11 shows this process. At a threshold of 20, the satellite peak at 5 ns is still seen in the timing difference distribution. At thresholds 30-50, the satellite peak begins to disappear; however, the count in the true coincidence peak at -5 ns starts to slightly decrease. At a T1 and T2 threshold of 60, shown in the lower left figure of Figure 4-11, the dark count induced peak completely disappears. Unfortunately, the true coincidence peak counts has decreased by almost an order of magnitude. A threshold of 40 was selected to use in all future measurements for the OGS arrays as it reduced satellite peak counts to less than 1% of the true coincidence peak without a significant reduction of counts in the true coincidence peak.

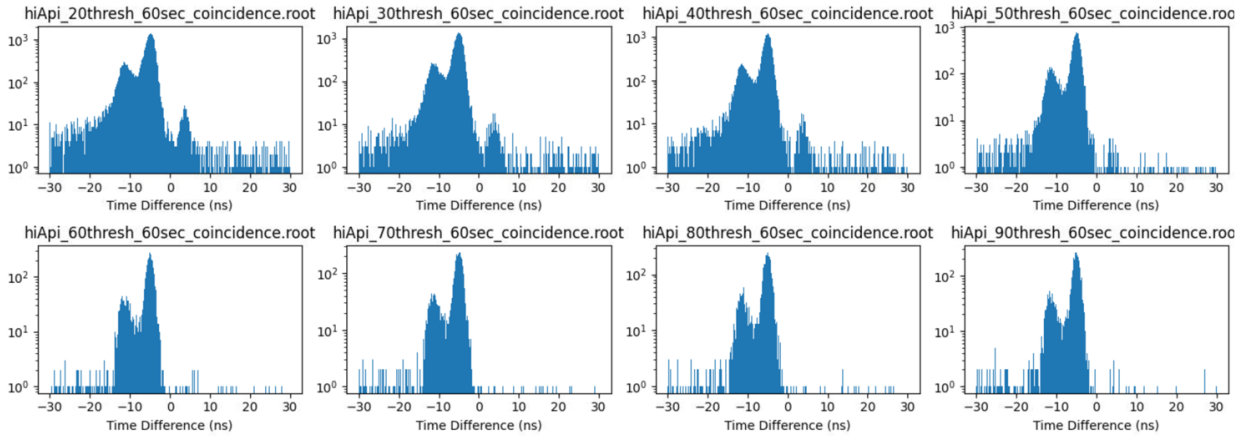

Figure 4-11. Increasing the threshold of the OGS array to remove satellite peak at a timing difference of 5 ns. Threshold starts at 20 and increases in increments of ten to a threshold of 90 in the lower right. Satellite peak completely disappears at a threshold of 60. Peak at -12 ns is the satellite peak from an incorrect threshold setting on the API Hamamatsu SiPM.

We used the same procedure to remove the satellite peaks caused by dark noise and the fe_delay mechanism for the Hamamatsu SiPM attached to the alpha screen of the D-T API neutron generator; the threshold was increased in increments of 10 from 30 to 60 with the resulting timing difference between the detected alpha particle and neutron shown in Figure 4-12 (Slight timing

shifts are exhibited between Figure 4-11 and 4-12 due to the use of extension cables in the experimental setup). Starting on the left, the satellite peak is present at -4 ns. Increase the threshold to 40 eliminates the satellite peak. Further increasing the threshold significantly reduces the coincident events recorded as the threshold is above the amount of light produced by interactions in the alpha screen. A threshold of 40 was selected for use in subsequent measurements for the d-t generator alpha screen SiPM.

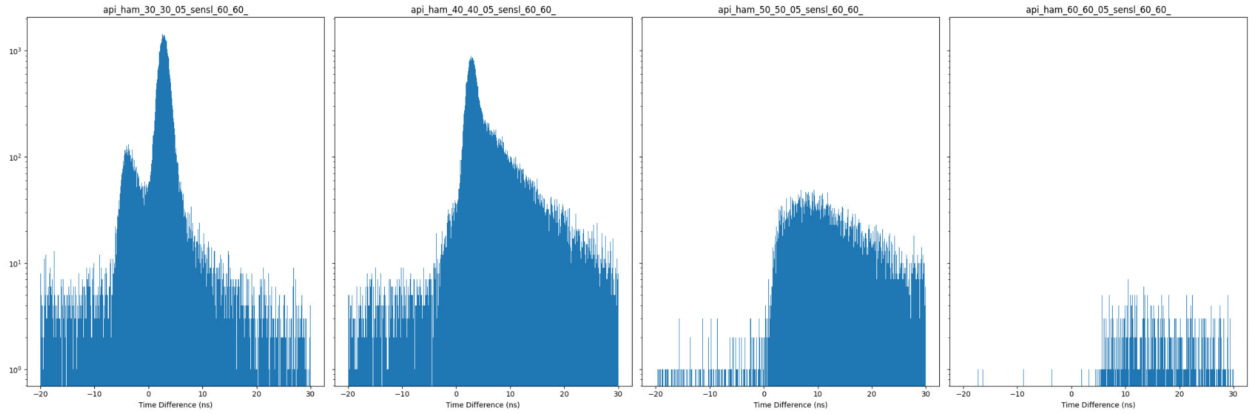

Figure 4-12. Increasing the detection threshold above errant dark noise to remove satellite peak. The timing difference between detected alpha particles and neutrons in the organic glass arrays is plotted starting with a threshold of 30 on the left and increase to a threshold of 60 on the right.

We used a Photek LPG-405 pulsed laser to uniformly illuminate the face of the SiPMs to determine the timing offsets. The LPG-405 pulsed laser is a 405 ns laser capable of pulse widths between 40-800 ps. We used SiPM 56 on the Hamamatsu S13361-3050AE-08 array as a reference for all other channels. Figure 4-13 shows the timing calibration setup inside a dark box. Due to the readout system's event size limit of 128 events (from the firmware version used at time of measurement), all channels cannot be simultaneously calibrated. Thus, the system was calibrated in steps: first the timing offsets between all pixels on the Hamamatsu S13361-3050AE-08 array were determined, along with the standard deviation of the timing difference. The T1 and T2 thresholds were optimized to obtain every laser pulse, while reducing satellite peaks to less than 1% of the main peak, as determined with prior testing using the API. For each run, it was confirmed that laser pulses were not lost during acquisition, which was observed to cause large timing offsets (up to 45 ns) that were possibly due to event mis-match due to exceeding the event size limit.

Figure 4-14 shows the resulting offsets from this first step. Overall, the timing offsets are within 2 ns with an outlier at -3.5 ns and the width of the timing distribution from the laser is centered around 250 ps. The timing widths are partially due to the laser pulse width combined with the time it takes each SiPM pixel to exceed threshold. Figure 4-15 shows the timing offset of each pixel on the SiPM. Signals originating from the left side of the Hamamatsu S13361-3050AE-08 SiPM reach the ASIC one to three nanoseconds before reference pixel 56. However, on the right side, the opposite is true where signals propagate to the ASIC slower than the reference pixel; the slower signal propagation is most likely due to design of the SiPM.

Next, each detector SiPM array was calibrated in reference to the same pixel (pixel 56) on the

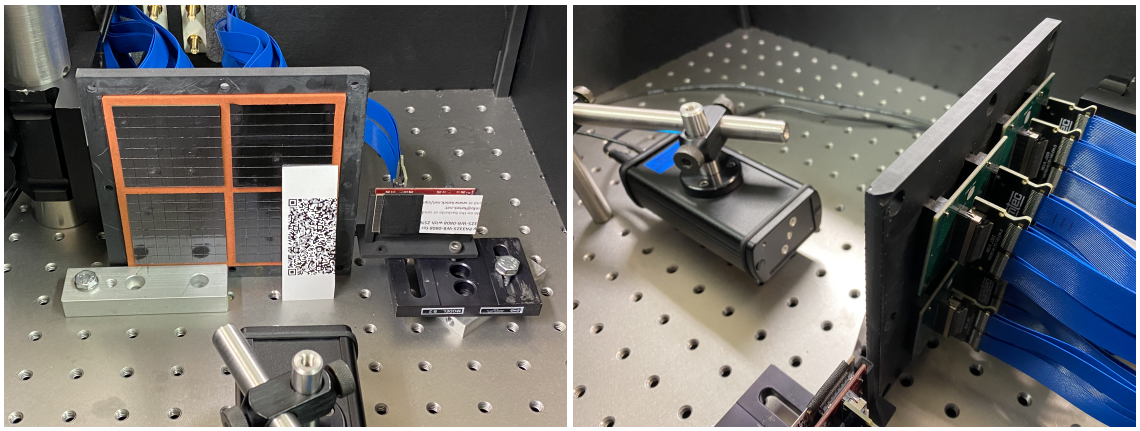

Figure 4-13. The time offset calibrations for all Hamamatsu S13361-3050AE-08 pixels relative to reference pixel 56.

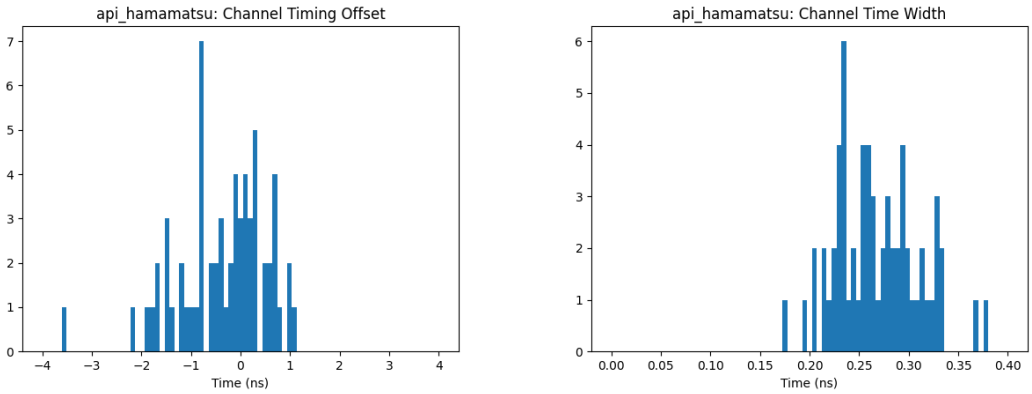

Figure 4-14. Timing calibration setup of the 2x2 array and single Hamamatsu S13361-3050AE-08 array using the Photek 405 laser.

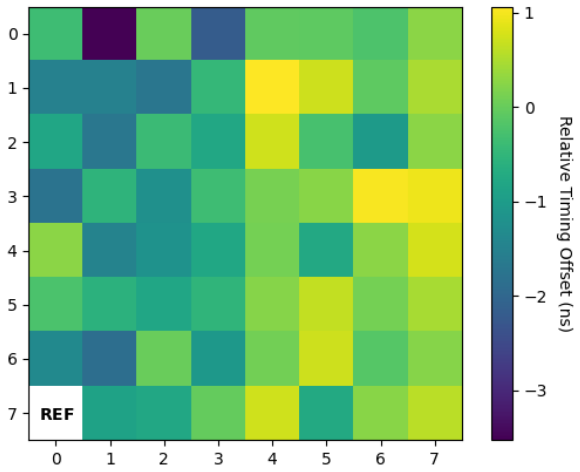

Figure 4-15. API timing offsets relative to pixel 56 (shown as REF in lower left)

Hamamatsu S13361-3050AE-08 array, with all but one row of the pixels masked to prevent exceeding the firmware event limit. Additionally, only two rows of each SensL/onsemi's ARRAYJ-60035-64P-PCB SiPM was calibrated at once. When attempting to calibrate more than two rows of pixels, shifts in increments of approximately 8 ns were observed (up to 45 ns).

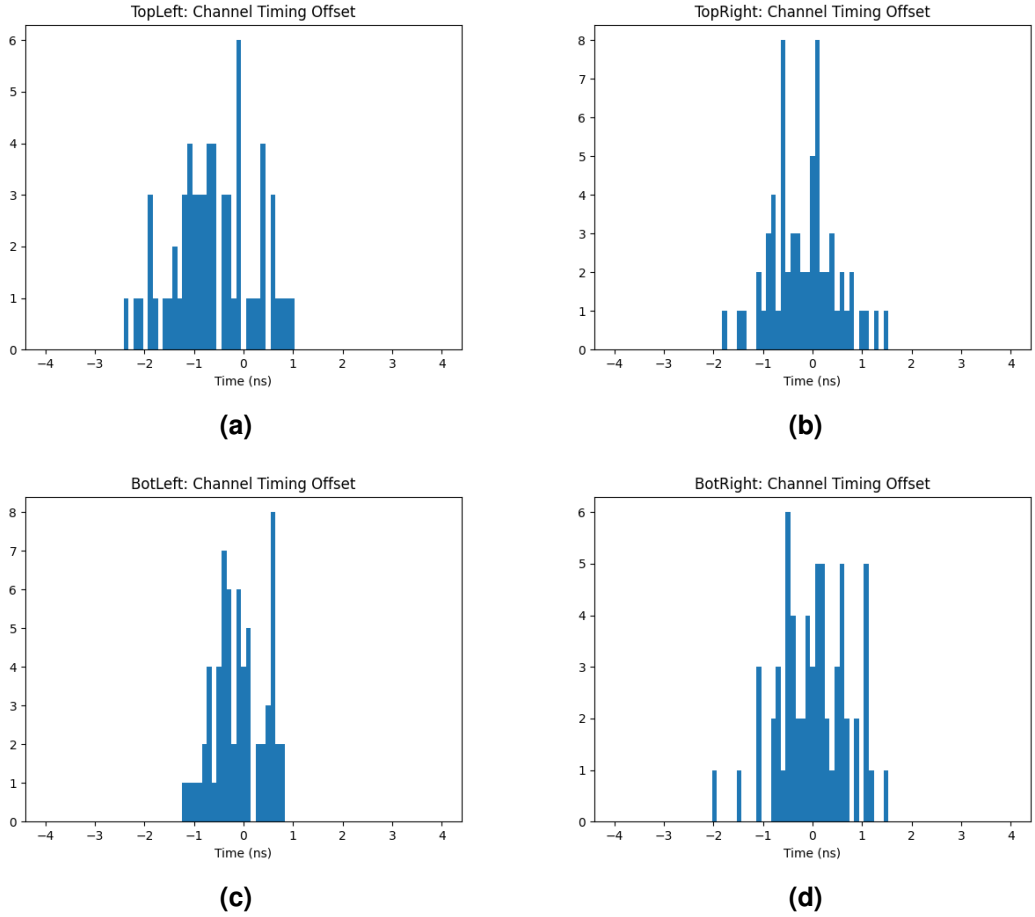

Figure 4-16. The time offset calibrations for all detector SiPM pixels, in reference to SiPM 56 on the Hamamatsu S13361-3050AE-08 array.

The taping of the Hamamatsu array and partial blocking of pixels from the SensL SiPM can be seen in Figure 4-13. Timing offsets for a complete SensL/onsemi's ARRAYJ-60035-64P-PCB SiPM were concatenated together from four different measurements. Figure 4-16 shows the resulting timing offsets for all four detector arrays, and Figure 4-17 shows the standard deviation of the time difference between the reference pixel and each detector pixel. One pixel had an offset of -24 ns. This pixel was not included for plotting purposes. Other than the outlier pixle, all time offsets are within 2 ns of the reference pixel, and the standard deviation is typically less than 200 ps as expected. In Figure 4-16, no discernible pattern emerges for the relative timing between the four different onsemi SiPM arrays.

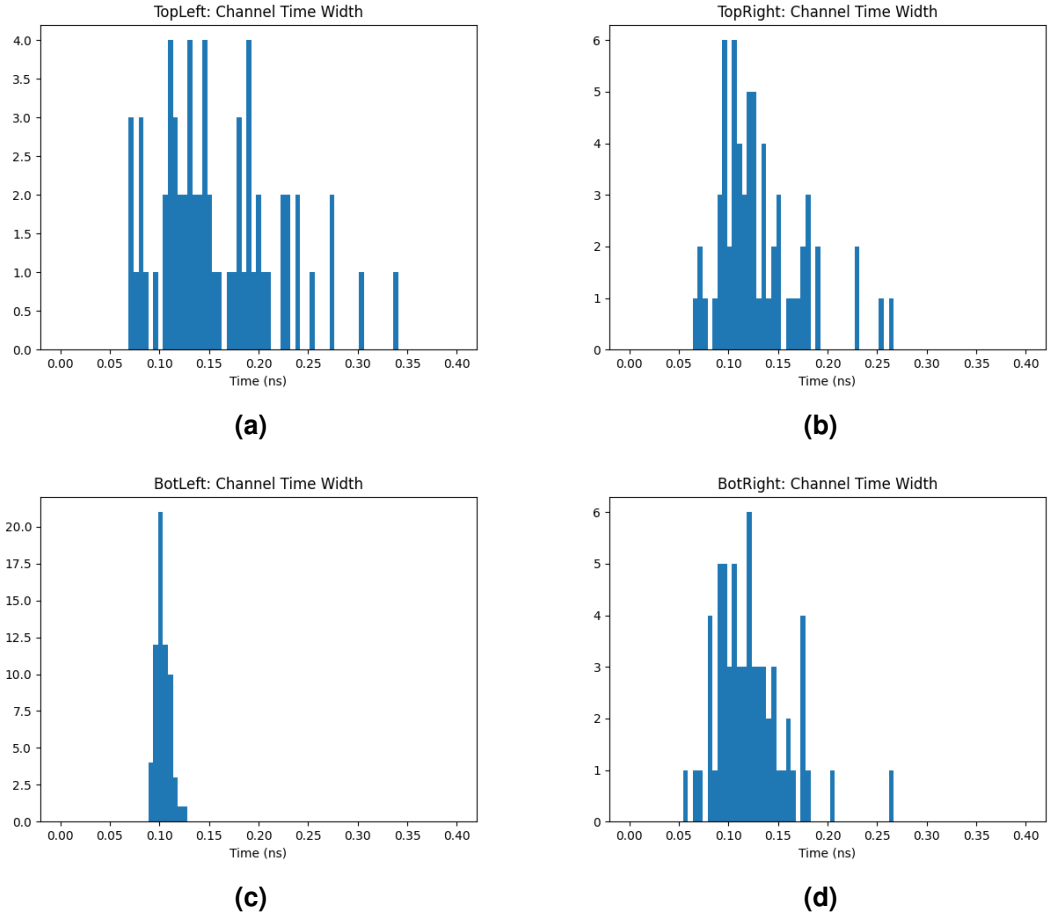

Figure 4-17. The standard deviation of the time difference between all detector SiPM pixels and SiPM 56 on the Hamamatsu S13361-3050AE-08 array.

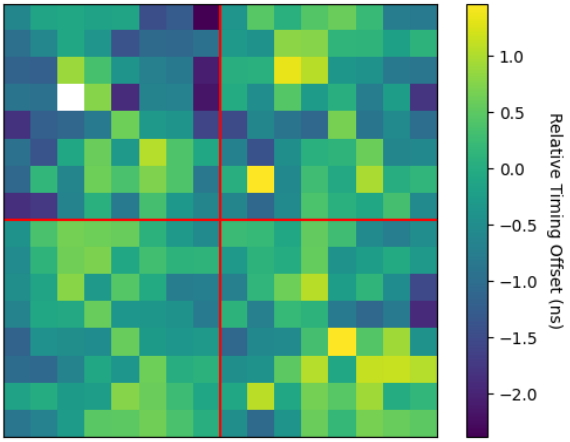

Figure 4-18. Timing offsets for all four SensL/onsemi's ARRAYJ-60035-64P-PCB SiPMs of the 2x2 array relative to pixel 56 on the the Hamamatsu S13361-3050AE-08 array. The red lines separate the four individual SiPM arrays. The white pixel in the upper left is the pixel that has an offset of approximately -24 ns. It was removed from this figure.)

4.2.2. Pixel Mapping, Uniformity

TOFPET2 software/hardware does not come with ASIC channel to SiPM pixel mapping. PetSys manufactures many types of FEB/S boards, so each user has to create their own custom ASIC channel to pixel mapping table relative to the SiPM and FEB/S combination being used. To verify we calculated the pixel map correctly, we plotted at a heat map of coincident API alpha screen hits on the Hamamatsu S13361-3050AE-08 array. The scintillation light produced in the alpha screen shows the approximate direction the alpha particle traveled after being created from the d-t interaction; the neutron created from this interaction traveled in the opposite direction. Generally, the hits on the API neutron generator alpha screen should centralized if we have placed the 2x2 OGS array near the center of the tagged neutron cone. Looking back at the measurement setup in Figure 4-5, one pixel on the alpha screen SiPM corresponds to a 3 cm (5 pixel) spot size at the OGS array; a single OGS array is approximately 5 cm wide, so a hot spot size corresponding to a two by two square of pixels is expected.

Figure 4-19 shows the heat map of coincident hits on the alpha screen for both before and after the pixel position correction is applied. Before the correction is applied on the left side of Figure 4-19, the hit position is indecipherable and no information should be concluded from the pixel hit intensities. However, after correcting for pixel position, the expected shape is seen in the heat map of coincident hits. The spot is larger than the two by two pixels expected due to noisy alpha screen waveforms (which is known from digitizing alpha screen waveforms for a past project).

A second and more concrete verification of correct pixel position used data from the masked timing calibration run of the Hamamatsu S13361-3050AE-08 array (show previously in Figure 4-13). During the measurement, only one row was exposed to the laser. Figure 4-20 shows a heat map of laser hits for the masked Hamamatsu S13361-3050AE-08 array. Light leaked one row

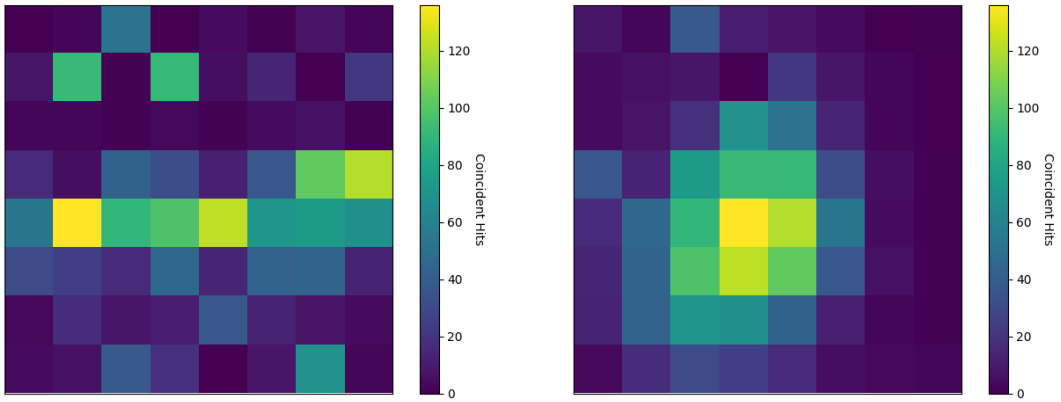

(a) (b)

Figure 4-19. Alpha screen hits above threshold. (a) Hit map without correction. (b) Hit map after correcting for pixel position.

further into the array and illuminated two rows of pixels rather than the desired one row. All other pixels did not record any hits from the laser pulses. This also shows that reference pixel 56 in the lower left corner is illuminated by the laser and can be used for timing offset calibrations.

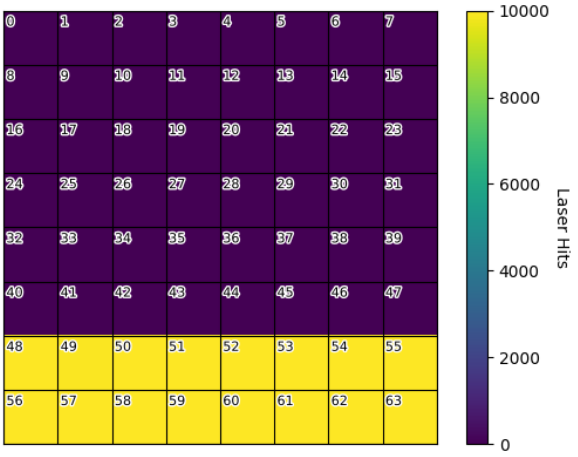

Figure 4-20. Heat map showing only two rows of the Hamamatsu S13361-3050AE-08 array receiving light from the laser for masked timing calibration measurements. The top 7 rows were masked with thick paper and tape. Light leaked one row further into the array than desired.

Figure 4-21 shows an 8x8 array of 8x8 heat maps. Each heat map corresponds to the hits on the API SiPM that were detected in a single OGS pixel. For example, the upper left plot (00) shows a heat map of hits on the alpha screen coincident with neutrons in pixel 00 of a single pixelated OGS arrays. As stated earlier, with 60 cm between the neutron generator and the 2x2 array, one 0.3 cm pixel of the Hamamatsu array corresponds to a five pixels of the 2x2 array. So, only a select few pixels should be contributing to hits of one of the OGS arrays. In general, the patterns

displayed in the figure agree that pixels from the upper left corner

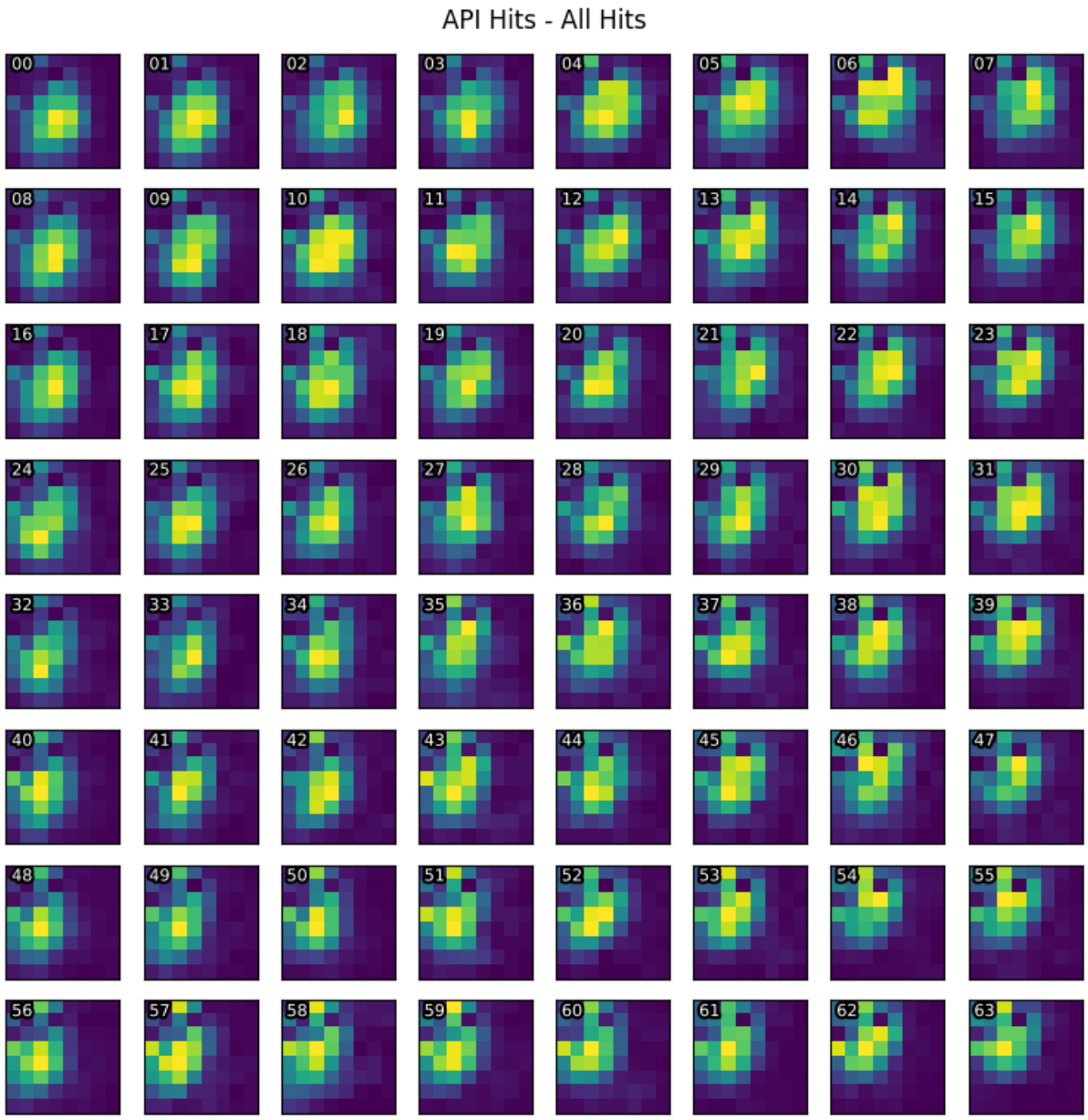

Figure 4-21. Coincident hits on the alpha screen from the API-120 Hamamatsu S13361-3050AE-08 array from a single pixelated OGS array. Each heat map shown indicates where a concident hit on the alpha screen exceeded threshold for a corresponding neutron interaction in the OGS array. For example, the upper left plot (00) shows a heat map of hits on the alpha screen coincident with neutrons in pixel 00 of one of the OGS arrays.

It is important to understand the response of each pixel to estimate how each one will react to incident scintillation light from alpha screen interactions or gamma/neutron energy depositions within the OGS pixelated array. Figure 4-22 shows the time over threshold distributions for each pixel on the API alpha screen. For this measurement, the threshold was set at values of 5, 15, 15 for T1, T2, and E respectively.

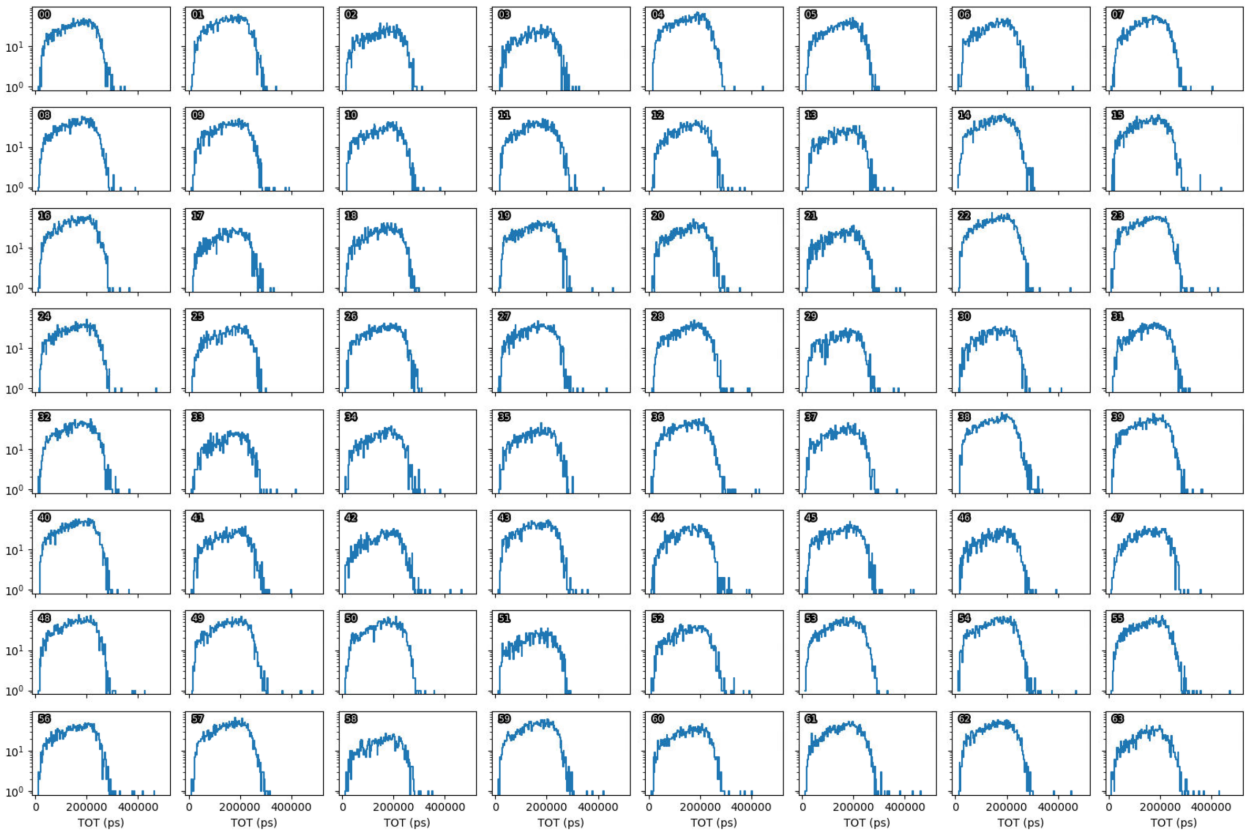

Figure 4-22. Hits on the API: Thresholds were set at (5, 15, 15) for (T1, T2, E). Highly uniform distributions are seen for each pixel of the API alpha screen SiPM.

There is good agreement in TOT shape and intensity between all pixels which demonstrates good uniformity and gain across the Hamamatsu S13361-3050AE-08 array. Some pixels show less intensity due to the positioning of the OGS array relative to the center of the alpha-tagged neutron cone from neutron generator. All pixels in the array show a threshold cutoff in the distribution at approximately the same TOT value. The API SiPM pixels are connected to a uniform alpha screen scintillator that is shipped with the d-t neutron generator. Any non-uniformity would be due to uneven optical grease application between the SiPM/alpha screen interface or gain variations inherent to the SiPM from manufacturing/ design.

The organic glass arrays, set at 60 cm from the d-t generator, are used to detect the neutron produced in the d-t interaction. Pixel uniformity of TOT values measured using the OGS arrays with ARRAYJ-60035-64P-PCB SiPMs has some additional complexity compared to the alpha screen. The organic glass arrays are made in-house at Sandia National Laboratories and are still undergoing research and development.

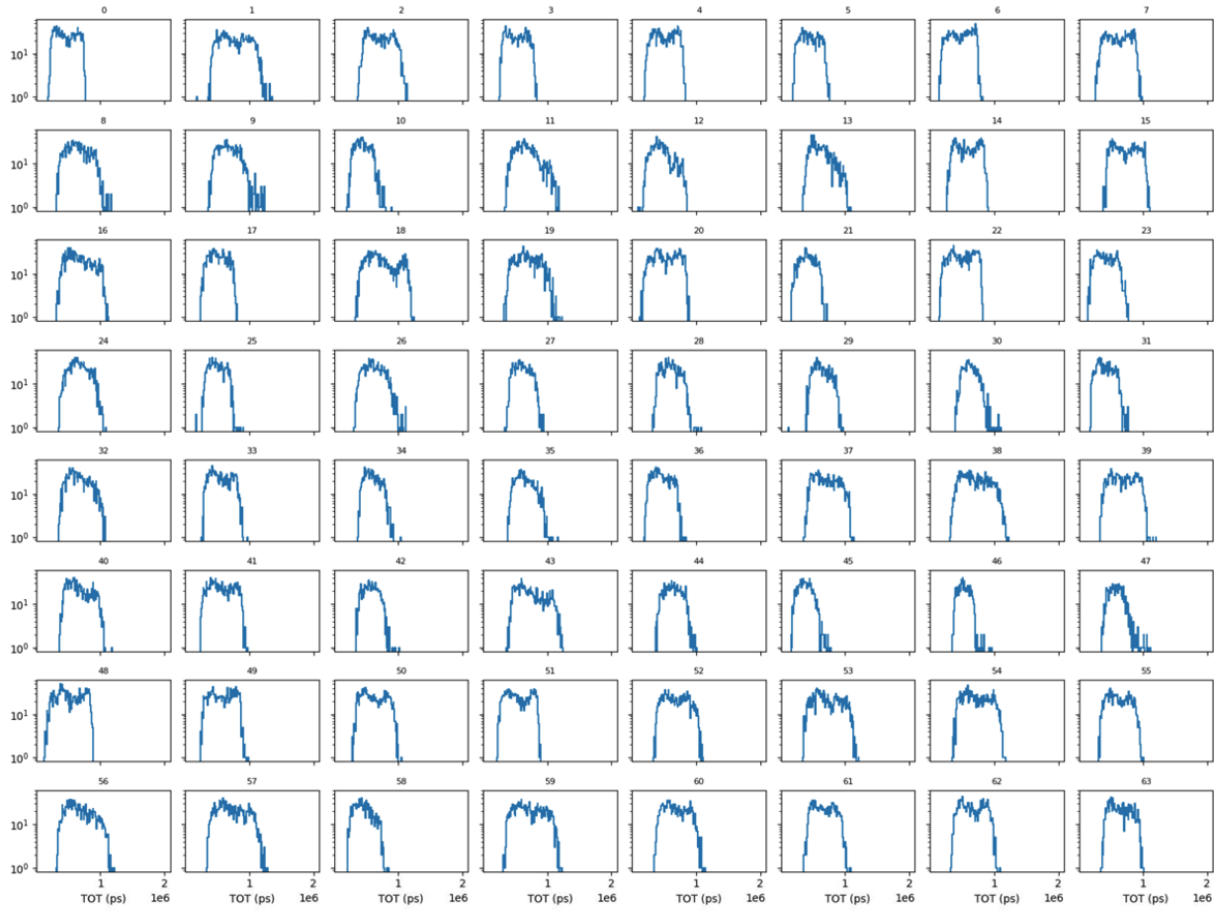

Figure 4-23. Hits on the detector: Thresholds were set at (20, 20, 20) for (T1, T2, E). Results shown are for an older version of the OGS array and not representative of what will be measured with the 2x2 array.

Figure 4-23 shows TOT values for each pixel a single pixelated organic glass scintillator array. The threshold for this measurement was set to (20, 20, 20). These results are from an older OGS

array design that was not used in the 2x2 array. These TOT histograms show less uniformity than the API TOT histograms from Figure 4-22, but that is expected.

There are many factors that can cause TOT differences. First issue is non-uniform light collection. Many pixel size of the OGS array is not consistent and some rows are smaller than the desired pixel size and some are larger. This size discrepancy allows scintillation light from one pixel to be shared with a neighboring pixel. Also, if the surface of the pixelated array is not completely flat, light loss occurs where air gaps are present in stead of optical grease. This causes total internal reflection of the scintillation light which reduces the signal measured by the SiPM. Air bubbles have been seen trapped within the OGS pixels which causes light collection issues.

Some TOT histograms shown in Figure 4-23 have lower threshold cutoffs such as pixel 10 and pixel 23. This could be caused by the threshold settings used for the measurement. The amplification of the signal from the "T" branch is larger than the amplification of the "E" branch. Therefore, a threshold of 20 for the "T" branch is lower than a threshold of 20 for the "E" branch. As stated before, the timing for TOT starts after the waveform surpasses the T2 threshold and stops after it goes below the threshold for "E". This could cause shifting and odd shapes in the TOT spectrum which is seen for a number of pixels.

5. DISCUSSION AND CONCLUSION

We have reported on the system response of a 2x2 array of pixelated organic glass scintillator detectors, each read out with the ARRAYJ-60035-64P-PCB Silicon Photomultiplier arrays and the TOFPET2-based readout system from PETsys Electronics. This system is a scaled down version of a API neutron radiography and computed tomography imaging system, for which we report on the expected imaging performance using simulated data in Geant4. The next scaled up version, shown in Figure 5-1, is for a 3x3 array. The energy and pulse-shape discrimination performance of 14 pixelated detectors is also characterized with full waveform digitization. The overall performance is consistent with an earlier characterization based on a pixelated detector with fins that did not allow close-packing: prior characterizations report the average light for all 64 pixels in one array at 340 keVee at 126$\pm$ 9 mV and a pulse shape discrimination figure-of-merit of 1.25$\pm$0.19. Nearly all recent detectors without fins are consistent with this result.

We also report on the timing and energy response of the 2x2 array read out with the TOFPET2-based system. Due to the unique triggering scheme in the TOFPET2 ASIC, careful calibration of the thresholds is required to avoid artifacts in the timing distribution. In addition, up to 1 ns offsets between ASIC channels required calibration with a time synced source. Finally, due to prior work showing the non-linearity of the QDC, we use the time-over-threshold out of the ASIC to measure the energy deposited. We show overall good uniformity from the API alpha scintillator screen, and attribute most non-uniformity in the organic glass detectors as being caused by the light transport in the pixels themselves.

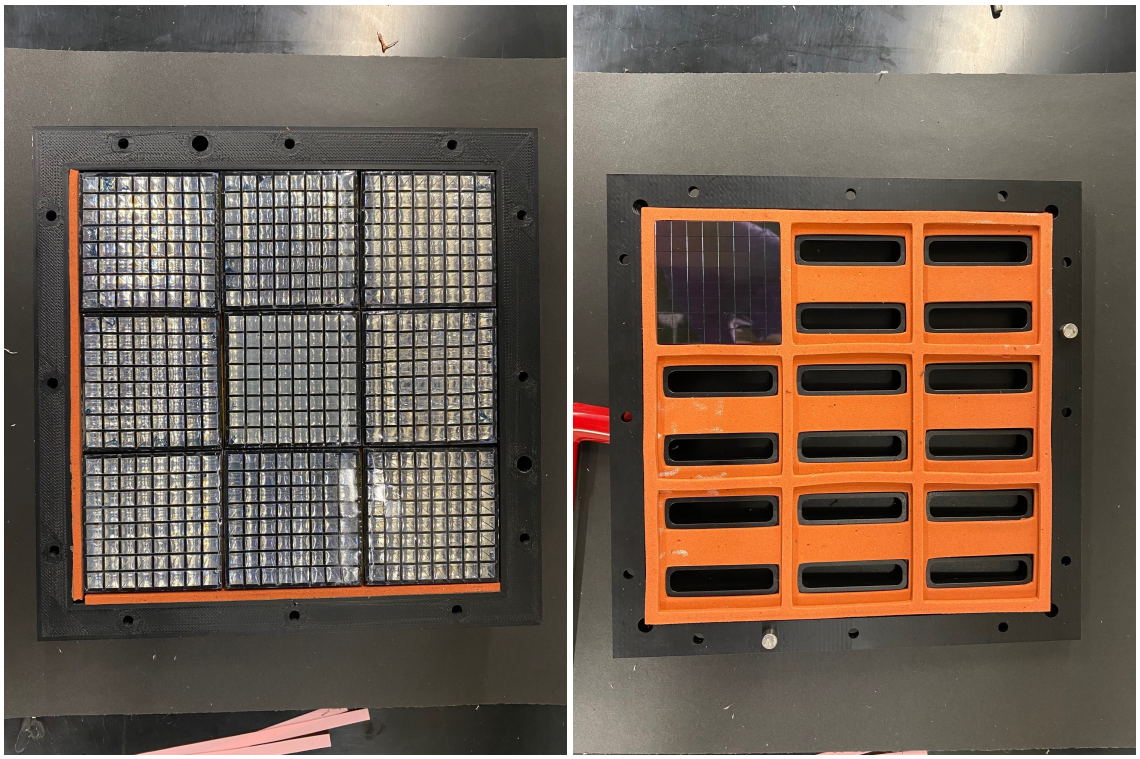

(a) (b)

Figure 5-1. The 3x3 array of detectors (a) and partially populated SiPM arrays (b).

REFERENCES

[1] P.A. Hausladen, M. A. Blackston, E. Brubaker, D.L. Chichester, P. Marleau, and R.J. Newby. *53rd Annual Meeting of the INMM, Orlando, FL*, 2012.

[2] R. J. Newby, P.A. Hausladen, M. A. Blackston, and J. F. Liang. *ORNL/TM-2013/82*.

[3] F. Habte, M. A. Blackston, P. A. Hausladen, and L. Fabris. *IEEE Nuclear Science Symposium Conference Record*, 2008.

[4] Paul A. Hausladen, Matthew A. Blackston, Deniz Aykac, John Sparger, Jens Gregor, Andrew J. Gilbert, Richard S. Wittman, and Erin A. Miller. 3d tomography and image processing using fast neutrons final report. *ORNL*, ORNL/SPR-2019/1418, 2020.

[5] H. O. Anger. *Review of Scientific Instruments*, 29:27–33, 1958.

[6] Martin Janecek and William W. Moses. Optical reflectance measurements for commonly used reflectors. *Transactions on Nuclear Science*, 55(4):2432–2437, 2008.

[7] M. Sweany, P. Marleau, S. Hammon, G. Kallenbach, and J.K. Polack. Design and evaluation of a pixelated psd-capable scintillator detector with sipm readout. *https://doi.org/10.2172/1560807*, 2019.

[8] Melinda Sweany, Patrick Feng, Mark Gerling, Paul Maggi, Peter Marleau, Lucas Nguyen, and Huu Tran. Performance evaluation of pixelated neutron detectors coupled to silicon photomultiplier arrays. *Sandia Internal Report*, SAND2021-12026, 2021.

[9] Joseph S. Carlson and Patrick L. Feng. Melt-cast organic glasses as high-efficiency fast neutron scintillators. *Nuclear Instruments and Methods in Physics Research Section A: Accelerators, Spectrometers, Detectors and Associated Equipment*, 832:152 – 157, 2016.

[10] Melinda Sweany, Liam Claus, John Mincey, and Peter Marleau. High channel count asic solutions for neutron detection: market survey and performance of the tofpet2 asic. *Sandia Internal Report*, SAND2020-11231, 2020.

[11] A. Di Francesco, R. Bugalho, L. Oliveira, L. Pacher, A. Rivetti, M. Rolo, J.C. Silva, R. Silvaa, and J. Varela. Tofpet2: a high-performance asic for time and amplitude measurements of sipm signals in time- of-flight applications. *Journal of Instrumentation*, 11(C03042), 2016.

[12] S. Agostinelli *et al.* Geant4 - a simulation toolkit. *Nuclear Instruments and Methods in Physics Research Section A: Accelerators, Spectrometers, Detectors and Associated Equipment*, 506:250–303, 2003.

[13] Hakan Erdoğan and Jeffrey A. Fessler. Monotonic algorithms for transmission tomography. *IEEE Transactions on Medical Imaging*, 18(9):801–813, 1999.

[14] R. Brun and F. Rademakers. Root - an object oriented data analysis framework. *Nuclear Instruments and Methods in Physics Research Section A: Accelerators, Spectrometers, Detectors and Associated Equipment*, 389:81–86, 1997.

[15] Nathan P. Giha, Marc L. Ruch, Angela Di Fulvio, William M. Steinberger, and Sara A. Pozzi. Readout electronics of a handheld dual particle imager. *IEEE Nucl. Sci. Symp. Atlanta, Ga*, 927:451 – 462, 2017.

[16] H. Klein and S. Neumann. Neutron and photon spectrometry with liquid scintillation detectors in mixed fields. *Nuclear Instruments and Methods in Physics Research Section A: Accelerators, Spectrometers, Detectors and Associated Equipment*, 476:132–142, 2002.

[17] M. Sweany, A. Galindo-Tellez, J. Brown, E. Brubaker, R. Dorrill, A. Druetzler, N. Kaneshige, J. Learned, K. Nishimura, and W. Bae. Interaction position, time, and energy resolution in organic scintillator bars with dual-ended readout. *Nuclear Instruments and Methods in Physics Research Section A: Accelerators, Spectrometers, Detectors and Associated Equipment*, 927:451 – 462, 2019.

[18] M.Sweany, P.Marleau, C.Allwork, G.Kallenbach, and S.Hammon. Characterization of a silicon photo-multiplier array with summing board as a photo-multiplier tube replacement in organic scintillator assemblies. *Nuclear Instruments and Methods in Physics Research Section A: Accelerators, Spectrometers, Detectors and Associated Equipment*, 953:163118, 2020.

[19] M.D. Rolo, L.N. Alves, E.V. Martins, A. Rivetti, M.B. Santosd, and J. Varelab. A low-noise cmos front-end for tof-pet. *Journal of Instrumentation*, 6(P09003), 2011.

[20] David Schug, Vanessa Nadig, Bjoern Weissler, Pierre Gebhardt, and Volkmar Schulz. Initial measurements with the petsys tofpet2 asic evaluation kit and a characterization of the asic tdc. *arXiv:*, 1808.05833v4, 2018.

DISTRIBUTION

Hardcopy—External

Number of Copies	Name(s)	Company Name and Company Mailing Address

Hardcopy—Internal

Number of Copies	Name	Org.	Mailstop

Email—Internal (encrypt for OUO)

Name	Org.	Sandia Email Address
Technical Library	1911	sanddocs@sandia.gov

Sandia National Laboratories

Sandia National Laboratories is a multimission laboratory managed and operated by National Technology & Engineering Solutions of Sandia LLC, a wholly owned subsidiary of Honeywell International Inc., for the U.S. Department of Energy's National Nuclear Security Administration under contract DE-NA0003525.